A Study on Nonlinear Optical Devices Based on One-Dimensional Photonic Crystal Cavity

Shuntaro Makino

Division of Media and Network Technologies
Graduate School of Information Science and Technology
Hokkaido University

Contents

Chapter 1 Introduction 1
Chapter 2 Formularization of the finite element method for periodic waveguide analysis 4
2.1 Introduction 4
2.2 2-D scalar finite element method for periodic waveguide 4
2.3 3-D vector finite element method for periodic waveguide 5
Chapter 3 Design of coupled ring resonator based on one-dimensional photonic crystal cavity 8
3.1 Introduction 8
3.2 Schematics of coupled ring resonator based on 1-D PC cavity 8
3.3 Transmission characteristics of coupled ring resonator based on 1-D PC cavity 9
3.4 Reduction of the number of periods in bending section 9
3.5 Conclusion 10
Chapter 4 Nonlinear characteristics of slot waveguide composed of one-dimensional photonic crystal cavity 13
4.1 Introduction 13
4.2 Schematic of slot waveguide composed of 1-D PC cavity 13
4.3 Structural dependence of effective refractive index and effective mode area 14
4.4 Investigation of nonlinear characteristics 14
4.5 Dependence of nonlinear coefficient on the number of holes 16
4.6 Conclusion 17
Chapter 5 Nonlinear characteristics of coupled resonator optical waveguide based on slotted one-dimensional photonic crystal cavity 25
5.1 Introduction 25
5.2 Schematic of CROW based on slotted 1-D PC cavity 25
5.3 Nonlinear characteristics of CROW based on slotted 1-D PC cavity 26
5.4 Slot-width dependence of nonlinear parameter 27
5.5 Conclusion 29
Chapter 6 Three-dimensional analysis of taper waveguide for highly-efficient connection between coupled resonator optical waveguide and straight waveguide 36
6.1 Introduction 36
6.2 Formulation of 3-D FETD-BPM 36
6.3 Confirmation of validity of 3-D FETD-BPM 38
6.4 Taper waveguide for highly-efficient connection between 1-D PC-CROW and straight waveguide 39
6.5 Conclusion 41

Chapter 7 Conclusion....48
Acknowledgements....50
References....51
Copyright notice....58
List of Author's Publication....59

Chapter 1 Introduction

Internet traffic is dramatically growing at approximately 30% per year because of the popularization of the high-speed mobile networks and the video-file sharing sites. According to the increase of Internet traffic, the power consumption of the network node for the routing is also climbing. The energy saving is a crucial matter for the future optical networks. The all-optical network, which is constructed of the optical devices instead of the electric devices, can reduce the energy consumption and realize the high-speed signal processing over the limit of the electric devices.

The nonlinear optical effects play a key role in the all-optical signal processing. However, the interaction between the light and the materials is generally weak. The high input power and the long physical length can enhance the interaction, however, the advantages of the optical waveguide, namely the low energy consumption and the high integrability, are lost. Recently, the slow light [1-4], which is the light with the small group velocity, has attracted much attention for the enhancement of the nonlinear optical effects. So far, the slow-light-enhanced nonlinear optical effects have been demonstrated, for example self-phase modulation (SPM) [5-8] and the four wave mixing (FWM) [9-13]. The slow light can be obtained at the band edge of photonic crystal (PC) waveguides, which are constructed of periodic dielectric materials [14-17]. The PC waveguides can offer the slow light on chip at the room temperature, however, the distortion of the optical pulse due to the large group velocity dispersion at the band edge is a crucial matter [18]. So far, the dispersion engineered PC waveguides [19-24], photonic crystal coupled waveguides (PCCW) [25-27], and the coupled resonator optical waveguides (CROWs) [28-32] are proposed to overcome the problem. In particular, the CROW is composed of the cascaded optical resonators along the propagation direction and can achieve zero group velocity dispersion at the center of its transmission band. In this study, the CROW based on the one-dimensional (1-D) PC cavity is investigated to enhance the nonlinear optical effects because it has the advantages in terms of the structural simplicity and the compactness compared with the two-dimensional (2-D) counterpart. The leakage loss of the general 1-D PC cavity constructed by removing holes of 1-D PC was large, however, the 1-D PC cavity based on the mode-gap confinement [33-36] proposed recently can realize high Q factor. The 1-D PC-CROW based on such high-Q cavity can achieve the small group velocity and the small leakage loss simultaneously [37]. In this study, the coupled ring resonator based on the 1-D PC-CROW is newly proposed toward the further decrease of the group velocity.

In addition to the small group velocity, the nonlinear optical effects are enhanced by the small effective mode area, which is the transverse energy density of the light. The slotted configuration is attractive for the small effective mode area because it can confine the light in the narrow region [38-

43]. Moreover, the high nonlinear materials can be employed as the low refractive-index cladding [44-46]. So far, the enhancement of the nonlinear optical effects in slot waveguides have been demonstrated, for example the FWM [47] and the stimulated Brillouin scattering (SBS) [48]. In this study, the slot waveguides based on 1-D PC cavity is proposed for the further enhancement of the nonlinear optical effects. Also, the PC structures with the slotted configuration are the promising structures for satisfying the high confinement of the light in the narrow region [49-75]. The CROW based on the slotted 1-D PC cavity is proposed and the enhancement due to the small group velocity and the small effective mode area is demonstrated. It can exceed the limit of the enhancement due to either the slow light or the small effective mode area. In general, there is the trade-off among the nonlinear optical effects, the leakage loss, and the bandwidth. The structural dependence of the group velocity and the leakage loss in the proposed structures is evaluated to find out the structural parameters that can realize the large optical nonlinear effect. Also, the nonlinear parameter, which is the figure of merit of the nonlinear optical effects, is calculated to evaluate the amplitude of the optical nonlinear effects quantitatively.

If the CROW structures are introduced to the optical circuits in practice, the optical pulse is launched from the straight waveguide. The taper waveguide is the essential component to realize the highly-efficient connection with the input waveguide over the wide bandwidth [76]. The three-dimensional (3-D) analysis of the taper waveguide is carried out first using the newly developed 3-D finite-element time-domain beam propagation method (FETD-BPM). The 3-D analysis is necessary for the consideration of the radiation to the vertical direction. The developed 3-D FETD-BPM is the powerful tool to design the optical waveguide in practice because it can evaluate the reaction of the optical pulse. The highly-efficient connection between the straight waveguide and the CROW structures over the wide bandwidth is demonstrated.

This thesis is structured as follows.

In this chapter, the background and the objective of this study are shown.

In chapter 2, the formularization of the finite element method (FEM) is presented. The results of this study are calculated using the FEM, which is a powerful tool for the electromagnetic field analysis. The solver based on the 2-D and 3-D FEM for the eigen-mode analysis is presented.

In chapter 3, the coupled ring resonator composed of the 1-D PC cavity is proposed. The structural parameters in terms of the trade-off between the group velocity and the leakage loss are demonstrated.

In chapter 4, the nonlinear characteristics of the slot waveguide composed of 1-D PC cavity is investigated. The appropriate waveguide-core structure is found out in terms of the balance of the effective mode area and the group velocity.

In chapter 5, the nonlinear characteristics enhanced by the slow-light effect of the CROW and the strong light confinement in the narrow region due to the slotted configuration are investigated. The appropriate slotted configuration in terms of the nonlinear coefficient and the leakage loss is

demonstrated.

In chapter 6, the taper waveguide for the highly-efficient connection between the CROW and the straight waveguide is investigated. The 3-D analysis of the taper waveguide is demonstrated, for the first time, using the newly developed 3-D FETD-BPM. The formularization of the 3-D FETD-BPM is also described.

In chapter 7, the findings of this study are summarized.

Chapter 2 Formularization of the finite element method for periodic waveguide analysis

2.1 Introduction

The numerical simulation in this study is performed by the FEM. The FEM is a powerful and efficient tool for the optical waveguide analysis because the analysis domain can be discretized inhomogeneously and adaptively according to the various optical waveguide structure. In this chapter, the FEM for the eigen-mode analysis of the 2-D and 3-D periodic waveguides [77, 78] is formulated.

2.2 2-D scalar finite element method for periodic waveguide

A 2-D periodic waveguide as shown in Fig. 2.1 is considered. From Maxwell's equations, the following wave equation can be obtained:

$$\frac{\partial}{\partial x}\left(p\frac{\partial \Phi}{\partial x}\right)+\frac{\partial}{\partial z}\left(p\frac{\partial \Phi}{\partial z}\right)+k_0^2 q\Phi=0 \tag{2.1}$$

with

$$\Phi=E_y,\ p=1,\ q=n^2 \quad \text{for TE mode} \tag{2.2}$$

$$\Phi=H_y,\ p=\frac{1}{n^2},\ q=1 \quad \text{for TM mode} \tag{2.3}$$

where E_y and H_y are the y-components of electric and magnetic fields, respectively, k_0 is free-space wavenumber, and n is the refractive index. The form of the solution is expressed as

$$\Phi=\phi\exp\left(-j\beta z\right) \tag{2.4}$$

where ϕ is the envelope of the electromagnetic field and β is propagation constant to the z direction. Dividing the analysis domain into the second-order triangular elements and applying the standard finite-element technique, the following equation can be obtained:

$$\left[\left[K\left(\beta\right)\right]+k_0^2\left[M\right]\right]\left\{\phi\right\}=\left\{u\right\} \tag{2.5}$$

with

$$\left[K\left(\beta\right)\right]=\sum_e\iint_e\left[\begin{array}{l} p\dfrac{\partial\left\{N\right\}}{\partial x}\dfrac{\partial\left\{N\right\}^T}{\partial x}+p\dfrac{\partial\left\{N\right\}}{\partial z}\dfrac{\partial\left\{N\right\}^T}{\partial z} \\ \quad -j\beta p\dfrac{\partial\left\{N\right\}}{\partial z}\left\{N\right\}^T+j\beta p\left\{N\right\}\dfrac{\partial\left\{N\right\}^T}{\partial z}+\beta^2 p\left\{N\right\}\left\{N\right\}^T \end{array}\right]dxdz \tag{2.6}$$

$$\left[M\right]=\sum_e\iint_e\left[q\left\{N\right\}\left\{N\right\}^T\right]dxdz \tag{2.7}$$

$$\{u\} = \int_{\Gamma_1} \{N\} p \frac{\partial \phi}{\partial z} dx + \int_{\Gamma_2} \{N\} p \frac{\partial \phi}{\partial z} dx \tag{2.8}$$

where $\{\phi\}$ is electric and magnetic field vector, $\{N\}$ is shape function vector, T denotes transpose, Σ_e denotes summation over all elements.

Applying the periodic boundary conditions based on Floquet theorem for the boundaries Γ_1 and Γ_2, the following equations are finally obtained:

$$\left[\left[\tilde{K}(\beta)\right] - k_0^2 \left[\tilde{M}\right]\right]\left\{\tilde{\phi}\right\} = \{0\} \tag{2.9}$$

with

$$\left\{\tilde{\phi}\right\} = \begin{bmatrix} \{\phi\}_0 \\ \{\phi\}_1 \end{bmatrix} \tag{2.10}$$

$$\left[\tilde{A}\right] = \begin{bmatrix} [A_{00}] & [A_{01}] + [A_{02}] \\ [A_{10}] + [A_{20}] & [A_{11}] + [A_{12}] + [A_{21}] + [A_{22}] \end{bmatrix} \tag{2.11}$$

where A represents K and M, the subscripts 1 and 2 denote the vector or matrix related to Γ_1 and Γ_2, respectively, and the subscript 0 denotes that for the remaining region.

2.3 3-D vector finite element method for periodic waveguide

A 3-D periodic waveguide as shown in Fig. 2.2 is considered. From the Maxwell's equations, the following vector wave equations are obtained:

$$\nabla \times \left([p] \nabla \times \mathbf{\Phi}\right) - k_0^2 [q] \mathbf{\Phi} = \{0\} \tag{2.12}$$

with

$$[p] = [\mu]_{PML}^{-1}, [q] = [\varepsilon]_{PML} \quad \text{for } \mathbf{\Phi} = \boldsymbol{E} \tag{2.13}$$

$$[p] = [\varepsilon]_{PML}^{-1}, [q] = [\mu]_{PML} \quad \text{for } \mathbf{\Phi} = \boldsymbol{H} \tag{2.14}$$

where $\boldsymbol{E}$ and $\boldsymbol{H}$ are the electric and magnetic field vectors, $[\varepsilon]_{\mathrm{PML}}$ and $[\mu]_{\mathrm{PML}}$ are the permittivity and permeability considering the PML. The form of the solution is expressed as

$$\mathbf{\Phi} = \boldsymbol{\phi} \exp(-j\beta z) \tag{2.15}$$

where $\boldsymbol{\phi}$ is the envelope of the electromagnetic field and β is propagation constant to the z direction. Dividing the analysis domain into the Linear Tangential / Quadratic Normal (LT/QN) tetrahedral edge elements and applying the standard finite-element technique, the following equation can be obtained:

$$\left[\left[K(\beta)\right] - k_0^2 [M]\right]\{\phi\} = \{u\} \tag{2.16}$$

with

$$\left[K(\beta)\right] = \sum_e \iiint_e \left(\nabla \times \{\boldsymbol{N}\}\right) \cdot \left([p] \nabla \times \{\boldsymbol{N}\}^T\right) d\Omega \tag{2.17}$$

$$\left[M\right]=\sum_{e}\iiint_{e}\left[q\right]\left\{\boldsymbol{N}\right\}\cdot\left\{\boldsymbol{N}\right\}^{T}d\Omega \tag{2.18}$$

$$\left\{u\right\}=\begin{Bmatrix}\left\{0\right\}\\ \sum_{e}\iint_{e}\left\{\boldsymbol{N}\right\}\cdot\left(n\times\left[p\right]\nabla\times\boldsymbol{\phi}\right)\Big|_{\Gamma_1}d\Gamma_1\\ -\sum_{e}\iint_{e}\left\{\boldsymbol{N}\right\}\cdot\left(n\times\left[p\right]\nabla\times\boldsymbol{\phi}\right)\Big|_{\Gamma_2}d\Gamma_2\end{Bmatrix} \tag{2.19}$$

where $\{\boldsymbol{\phi}\}$ is electric and magnetic field vector, $\{N\}$ is shape function vector, T denotes transpose, Σ_e denotes summation over all elements.

Applying the periodic boundary conditions based on Floquet theorem for the boundaries Γ_1 and Γ_2, the following equations are finally obtained:

$$\left[\left[\tilde{K}\left(\beta\right)\right]-k_0^2\left[\tilde{M}\right]\right]\left\{\tilde{\phi}\right\}=\left\{0\right\} \tag{2.20}$$

with

$$\left\{\tilde{\phi}\right\}=\begin{bmatrix}\left\{\phi\right\}_0\\ \left\{\phi\right\}_1\end{bmatrix} \tag{2.21}$$

$$\left[\tilde{A}\right]=\begin{bmatrix}\left[A_{00}\right] & \left[A_{01}\right]+\left[A_{02}\right]\\ \left[A_{10}\right]+\left[A_{20}\right] & \left[A_{11}\right]+\left[A_{12}\right]+\left[A_{21}\right]+\left[A_{22}\right]\end{bmatrix} \tag{2.22}$$

where A represents K and M, the subscripts 1 and 2 denote the vector or matrix related to Γ_1 and Γ_2, respectively, and the subscript 0 denotes that for the remaining region.

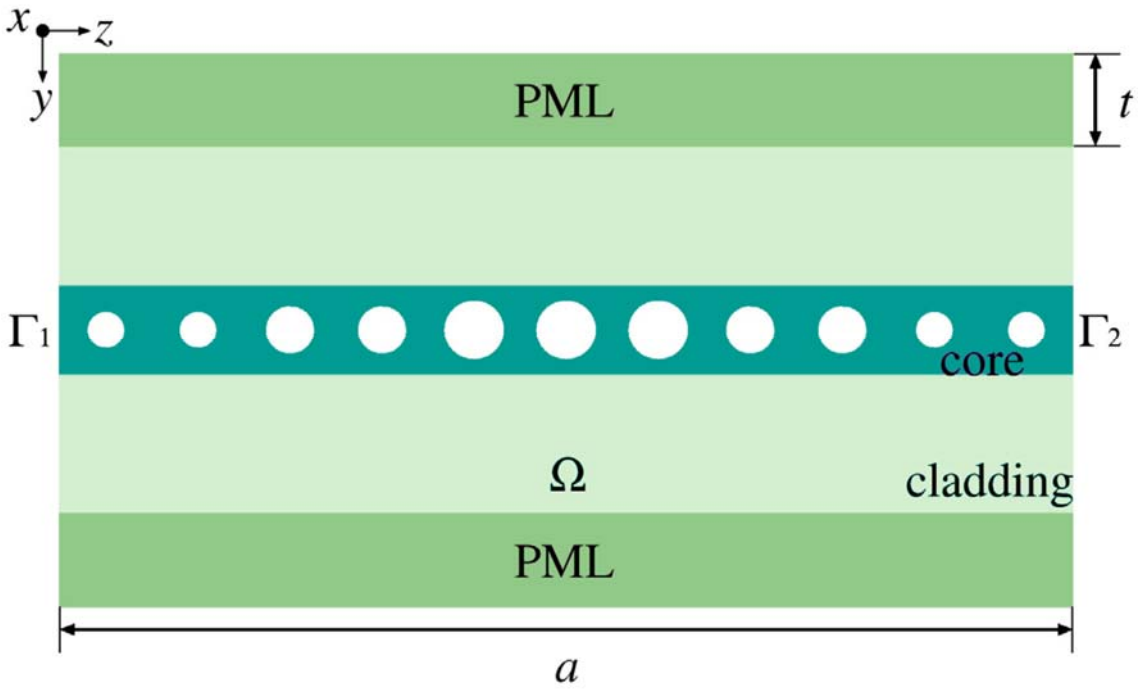

Fig. 2.1 A 2-D periodic waveguide.

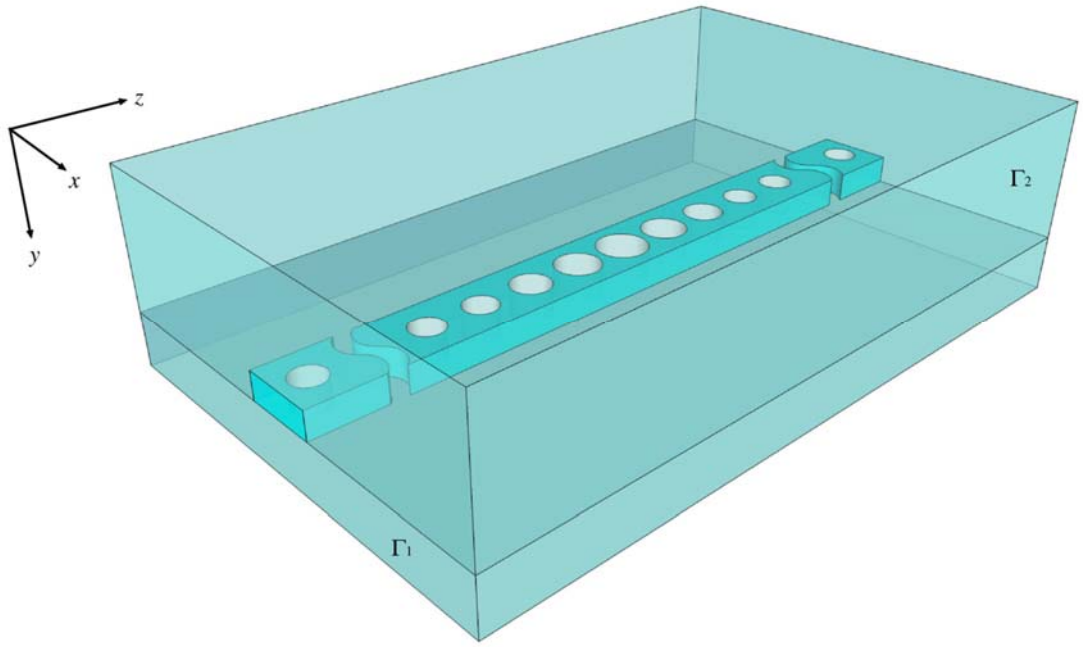

Fig. 2.2 A 3-D periodic waveguide.

Chapter 3 Design of coupled ring resonator based on one-dimensional photonic crystal cavity

3.1 Introduction

Slow light, which is the light with the small group velocity, has attracted much attention for the enhancement of the optical nonlinear effects. The PC waveguides can realize the slow light at room temperature. However, the group velocity dispersion, which leads the optical pulse to broadening, has to be considered. In many concepts of engineering the dispersion, the CROW is highly attractive because it can realize the zero group velocity dispersion at the center of its transmission band. The CROW is composed of cascaded resonators along the propagation direction and the light propagates by the coupling between neighboring resonators. The CROW based on the high-Q PC cavity has an advantage in terms of the photonic integration. In particular, the 1-D PC-CROW based on photonic wires is attractive because its structure is simple and compact in comparison with higher dimensional PC-CROW. However, the conventional 1-D PC-CROW, which is constructed by removing air holes in 1-D PC periodicity, has large leakage losses. The leakage losses can be suppressed by tailoring the envelope of electromagnetic distribution to fit Gaussian function. In order to suppress the leakage loss and realize the high-Q factor, 1-D PC cavity based on the modulated mode-gap barriers is proposed. The 1-D PC-CROW based on such high-Q 1-D PC cavity can realize the small group velocity and the low leakage losses simultaneously. In this chapter, the coupled ring resonator composed of the 1-D PC-CROW is newly proposed to furthermore decrease the group velocity. The transmission characteristics of the proposed structure is investigated using 2-D FEM for periodic waveguide analysis. The structural parameters in terms of the trade-off between the group velocity and the leakage loss are demonstrated.

3.2 Schematics of coupled ring resonator based on 1-D PC cavity

Fig. 3.1(a) shows the schematics of the coupled ring resonator based on the 1-D PC cavity. The ring resonators are placed side by side. The core and the cladding materials are assumed as the Si and the SiO_2. The distance between the ring resonators is d = 150, 200, and 220 nm for m = 4, 5, and 6. The one-period length of the coupled ring resonators is Λ_a. A red circle in Fig. 3.1(a) represents a 1-D PC cavity as shown in Fig 3.1(b). The coupling section has two periods of the 1-D PC cavity and the 90-degree bend section has 3 periods of the 1-D PC cavity. The waveguide parameters of the 1-D PC cavity are set as follows: The waveguide width w = 540 nm and the lattice constant a = 400 nm. The

number of the air holes is $2m$+1 and the one-period length of the 1-D PC cavity is $\Lambda_b = (2m+1)a$. In this study, the structural dependence for m = 4, 5, and 6 is investigated. All the air holes are numbered as shown in Fig. 3.1(b) and the i-th air hole radius is calculated by the following function:

$$r_i = r_0 \left\{ 1 - \left(\frac{i}{M_r} \right)^2 \right\}, \tag{3.1}$$

where r_0 = 120 nm is the air hole radius at the center of the resonator and M_r = 19, 21, and 21 for m = 4, 5, and 6 are the value that controls the changing ratio of the air hole radius. Moreover, the minimum air hole radius r_{min} is set as 115 nm to realize the small group velocity and the low leakage loss simultaneously. If the calculated r_i is smaller than r_{min}, r_i is replaced as r_{min} value.

3.3 Transmission characteristics of coupled ring resonator based on 1-D PC cavity

The 2-D FEM for the periodic waveguide analysis is applied to the coupled ring resonator based on the 1-D PC cavity. The Table 3.1 shows the normalized group velocity and the leakage loss of the coupled ring resonator and the 1-D PC-CROW at the wavelength that realize the zero group velocity dispersion. The leakage loss is calculated as

$$Leakage\ loss = 8.686 \times \left| \mathrm{Im}\left\{ \beta \right\} \right|, \tag{3.2}$$

where Im $\{\beta\}$ is the imaginary part of the propagation constant, which is given by

$$\mathrm{Im}\left\{ \beta \right\} = \frac{\mathrm{Im}\left\{ \omega \right\}}{v_g}, \tag{3.3}$$

where Im $\{\omega\}$ is the imaginary part of the angular frequency [79]. The group velocity of the CROW is governed by the strength of the coupling between the neighboring resonators. Since the structure with the large m-value has the long distance between the neighboring resonators, the strength of the coupling becomes weak. Therefore, the normalized group velocity decreases as the number of holes increases. As a result, we can confirm that the coupled ring resonator has smaller group velocity than the 1-D PC-CROW. However, the leakage loss of the coupled ring resonator is larger than the 1-D PC-CROW because of the bending section. Therefore, the m-value have to be chosen carefully in terms of the trade-off between the group velocity and the leakage loss. Fig. 3.2 shows the electromagnetic field distribution with m = 5 at the wavelength that realize the zero group velocity dispersion. The coupling with the each 1-D PC cavity can be seen.

3.4 Reduction of the number of periods in bending section

In the previous section, the small group velocity of the coupled ring resonator based on 1-D PC cavity is demonstrated. In this section, the reduction of the number of periods in the 90-degree bend section

is considered for the downsizing footprint. Table 3.2 shows the normalized group velocity and the leakage loss of the coupled ring resonators, whose 90-degree bend sections are composed of 1, 2, and 3 periods of 1-D PC cavity. The small group velocity is maintained while the number of periods in 90-degree bend section decreases. However, the leakage loss increases since the bending radius becomes sharp. The 2 periods of 1-D PC cavity is preferable for composing the 90-degree bent section in consideration of the trade-off among the leakage loss, the footprint and the group velocity.

3.5 Conclusion

A coupled ring resonator based on 1-D PC cavity is proposed and investigated its transmission characteristics by using 2-D FEM for periodic waveguide analysis. In order to suppress the leakage loss, the 1-D PC cavity with mode-gap confinement is employed. The small group velocity of the coupled ring resonator based on 1-D PC cavity is demonstrated, moreover, the reduction of the number of periods in 90-degree bend section is considered for the downsizing footprint. The advantageous of the 90-degree bend waveguide composed of 2 periods is demonstrated.

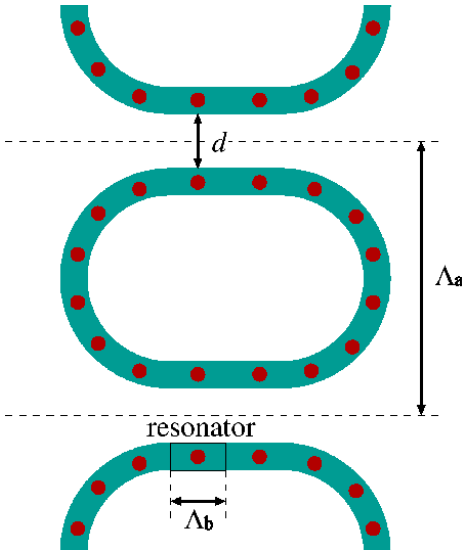

(a)

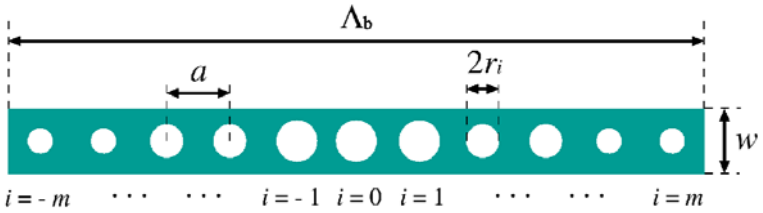

(b)

Fig. 3.1 Schematic of (a) the coupled ring resonator and (b) 1-D PC cavity.

Table 3.1

Normalized group velocity and leakage loss of 1-D PC-CROW and coupled ring resonator.

	m	v_g/c	Leakage loss [dB/mm]
1-D PC-CROW	4	0.131	1.39×10^{-4}
	5	0.101	6.11×10^{-4}
	6	0.081	2.17×10^{-3}
Coupled ring resonator	4	0.053	8.50×10^{-2}
	5	0.036	1.85×10^{-1}
	6	0.033	9.80×10^{-2}

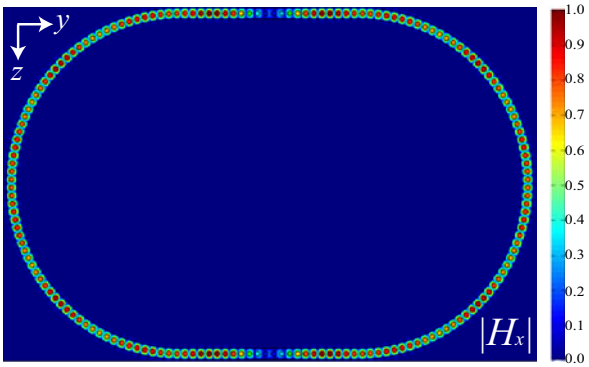

Fig. 3.2 Electromagnetic field distribution for $m = 5$.

Table 3.2

Normalized group velocity and leakage loss of coupled ring resonator. The 90-degree bend waveguide is composed of 1, 2, and 3 periods of 1-D PC cavity.

	m	v_g/c	Leakage loss [dB/mm]
3 periods	4	0.053	8.50×10^{-2}
	5	0.036	1.85×10^{-1}
	6	0.033	9.80×10^{-2}
2 periods	4	0.056	2.65×10^{-1}
	5	0.040	6.09×10^{-1}
	6	0.034	6.64×10^{-1}
1 periods	4	0.046	1.09×10^{2}
	5	0.035	8.89
	6	0.028	8.57

Chapter 4 Nonlinear characteristics of slot waveguide composed of one-dimensional photonic crystal cavity

4.1 Introduction

Slot waveguides have attracted much attention because of their unique property of strongly confining light to the low-refractive-index and narrow region [38-43]. By filling the slot region with a material that has the high nonlinear refractive index, nonlinear optical effects can be effectively enhanced [44-46]. The enhancement of the nonlinear optical effects in slot waveguides have been demonstrated; for example the FWM [47] and the stimulated Brillouin scattering (SBS) [48]. On the other hand, PC waveguides have also been studied for the enhancement of the optical nonlinear effects since the small group velocity of PC waveguides provides the strong interaction between the light and the materials. The slow-light-enhanced nonlinear optical effects have been demonstrated, for example self-phase modulation (SPM) [5-8] and the four wave mixing (FWM) [9-13].

Recently, the several types of combinations of the slot waveguides and PC waveguides have been reported [56, 69, 73-75]. By using these combined structures, both strong light confinement and slow-light effects can be obtained. The slow-light-enhanced optical nonlinearity in the slotted 2-D PC waveguides was experimentally studied [69], and electro-optic modulator [74] and absorption spectrometer [75] were proposed. Also, the horizontally slotted 1-D PC cavity for lasing was demonstrated [61]. Riboli *et al.* proposed basic concepts of the slot waveguides composed of 1-D PC cavity [73]. However, slow-light-enhanced nonlinear characteristics of the slot waveguides composed of the PC cavity have not been investigated yet. In this chapter, the slow-light-enhanced nonlinear characteristics of the slot waveguides composed of 1-D PC cavity is investigated. In order to realize the high confinement of the light, 1-D PC cavity based on the modulated mode-gap barrier [33-36] is employed. Using the 3-D vector FEM for periodic waveguide analysis [78, 80], the effective nonlinear coefficient of the proposed structure is evaluated. The numerical results show that the high nonlinear coefficient can be obtained by optimizing the waveguide width and height. Moreover, the trade-off between the nonlinear coefficient and the bandwidth is also discussed in the case of changing the number of holes.

4.2 Schematic of slot waveguide composed of 1-D PC cavity

Fig 4.1 shows a schematic of the slot waveguides composed of 1-D PC cavity, where a is a lattice constant, w is a waveguide width, h is a waveguide height, and w_s is a slot width. Fig. 4.2 shows a

cross section of the slot waveguide. The slot region is composed by sandwiching a cladding material between two 1-D PC cavity. The core, under-cladding, and over-cladding materials are assumed as Si, SiO_2 and DDMEBT [81]. DDMEBT can homogenously fill a slot region and holes because of its molecule structure in practice. The refractive indices of Si, SiO_2, and DDMEBT are set as 3.5, 1.45, and 1.8, respectively. All the holes in the 1-D PC cavity are numbered as shown in Fig. 4.1. The number of holes is $2m$+1 and the one-period length is $\Lambda = (2m+1)a$. The i-th hole radius r_i is calculated as

$$r_i = r_0 \left\{ 1 - \left(\frac{i}{M_r} \right)^2 \right\}, \tag{4.1}$$

where r_0 is the hole radius at the center of the 1-D PC cavity and M_r is a value that controls a changing ratio of the hole radius. Moreover, the minimum air hole radius $r_{\min}$ is set as 115 nm to realize the small group velocity and the low leakage loss simultaneously. If the calculated r_i is smaller than $r_{\min}$, r_i is replaced as $r_{\min}$ value. From the results of previous works [37], each waveguide parameters are set as m = 6, r_0 = 100 nm, M_r = 19, and $r_{\min}$ = 90 nm in order to achieve the small group velocity and low leakage loss simultaneously.

4.3 Structural dependence of effective refractive index and effective mode area

The structural dependence of the effective refractive index and the effective mode area of the slot waveguide as shown in Fig. 4.2 is investigated using 2-D VFEM [82]. The waveguide width w and height h are changed from 150 nm to 350 nm. The slot width w_s is fixed as 100 nm. Fig. 4.3(a) and (b) show the effective refractive index and the effective mode area as a function of the waveguide width for the different waveguide height. Fig. 4.4(a) and (b) show the electromagnetic field distributions of the slot waveguides that achieve small effective mode area ($w = h$ = 250 nm) and large effective mode area ($w = h$ = 350 nm). It can be seen that the effective refractive index increases as the waveguide width and height increase. On the other hand, it can be seen that the effective mode area changes as a quadratic function. In short, the effective mode area has a minimum value in specific waveguide parameters. If the enhancement of the optical nonlinear effects of conventional slot waveguides is considered, the smallness of the effective mode area is important. However, the enhancement of optical nonlinearity in the slot waveguide composed of 1-D PC cavity has to be evaluated in terms of the effective mode area and the group velocity.

4.4 Investigation of nonlinear characteristics

The structural dependence of the nonlinear coefficient is investigated using 3-D VFEM for periodic waveguide analysis [78, 80]. From the results of previous section, three combinations of the waveguide

width and height $w = h$ = 250 nm, 300 nm, and 350 nm is chosen since the waveguide width w is needed to be larger than $2r_i$. Fig. 4.5(a)-(c) show the structural dependence of the dispersion curves, the group index, and the leakage losses of the slot waveguides composed of 1-D PC cavity, where β is the propagation constant along the propagation direction, and n_g is the group index. Fig. 4.6 shows the electromagnetic field distribution of the slot waveguides composed of 1-D PC cavity with $w = h = 350$ nm. The strong confinement in the slot region can be seen. The group index at a frequency that achieves the zero group velocity dispersion gets larger as the waveguide width and height increase as shown in Fig. 4.5(b). The group index at the frequency that achieves the zero group velocity dispersion is 4.4, 5.3, and 5.6 for $w = h$ = 250 nm, 300 nm, and 350 nm, respectively. The leakage losses is calculated as

$$Leakage\ loss = 8.686 \times \left|\mathrm{Im}\left\{\beta\right\}\right|, \tag{4.2}$$

where Im $\{\beta\}$ is the imaginary part of the propagation constant, which is given by

$$\mathrm{Im}\left\{\beta\right\} = \frac{\mathrm{Im}\left\{\omega\right\}}{v_g}, \tag{4.3}$$

where Im $\{\omega\}$ is the imaginary part of the angular frequency [79]. The leakage losses at the frequency that achieves zero group velocity dispersion gets larger as the waveguide width and height decrease. This is because the effective refractive index becomes close to the refractive index of over-cladding if the waveguide width and height decrease as shown in Fig. 4.3(a). The nonlinear characteristics of the slot waveguide composed of 1-D PC cavity is evaluated by calculating its nonlinear coefficient γ. The nonlinear coefficient is defined as the following function [7, 8]:

$$\gamma = \frac{2\pi n_2 S^2}{\lambda A_{eff}} \tag{4.4}$$

where λ is an operation wavelength, A_{eff} is the effective mode area, n_2 is a nonlinear refractive index, and S is a slowdown factor. The mode geometry of the slot waveguides composed of 1-D PC cavity is assumed to be uniform along propagation direction; therefore, the effective mode area of the slot waveguide composed of 1-D PC cavity is calculated as $A_{\mathrm{eff}} = V_{\mathrm{eff}} / \Lambda$ [12, 13], where Λ is the one-period length and V_{eff} is the effective mode volume defined as

$$V_{eff} = \frac{\iiint \varepsilon\left(x,y,z\right)\left|\boldsymbol{E}\left(x,y,z\right)\right|^2 dxdydz}{\max\left[\varepsilon\left(x,y,z\right)\left|\boldsymbol{E}\left(x,y,z\right)\right|^2\right]}. \tag{4.5}$$

The slowdown factor is calculated using the results of the group index mentioned above, $S = n_g/n_{\mathrm{DDMEBT}}$. The nonlinear refractive index of DDMEBT is assumed as $n_2 = 1{:}7 \times 10^{-17}$ m^{2}W^{-1} [81]. The effective mode area, the group index, the square of the slowdown factor, and the nonlinear coefficient at the frequency that achieves zero group velocity dispersion are summarized in Table 4.1. The effective mode area becomes small as the waveguide width and height get smaller. On the other

hand, the group index becomes large as the waveguide width and height get larger. The ideal condition is to make the effective mode area smaller and the group index larger, however, there is the trade-off between the effective mode area and the group index. We consider that such trade-off is caused by the following reason. When the effective mode area becomes small, from Fig. 4.4(a), we can see that the electric field is strongly confined in the narrow slot region. On the other hand, when the effective mode area becomes large, the electric field spreads throughout the slot waveguide as shown in Fig. 4.4(b). The strong electromagnetic field distributions in the 1-D PC cavity makes the group index large. As a result, there is no parameters that satisfy the smallest effective mode area and the largest group index simultaneously. When the enhancement of the optical nonlinear effects in slot waveguides is considered, the small effective mode area is important to realize the strong light confinement in a narrow slot region. On the other hand, when the enhancement of the optical nonlinear effects in PC waveguides, the large group index is important to increase the light-matter interactions. However, in the case of the slot waveguides composed of 1-D PC cavity, the nonlinear coefficient does not become maximum in the structure that achieves the smallest effective mode area or the largest group index as shown in Table 4.1. As a results, it is essential to explore the optimum waveguide width and height for the enhancement of the optical nonlinear effects by investigating the structural dependence of the nonlinear coefficient. The largest nonlinear coefficient can be obtained $\gamma_{\mathrm{eff}} = 11\ 600\ \mathrm{m^{-1}W^{-1}}$ for $w = h = 300$ nm as shown in Table 4.1.

4.5 Dependence of nonlinear coefficient on the number of holes

For further evaluation of the nonlinear characteristics, the dependence of the nonlinear coefficient on the number of holes in 1-D PC cavity in this section. The following waveguide parameters are used; waveguide width and height $w = h = 300$ nm, $M_r = 11$, 15 and 19 for $m = 4$, 5 and 6, respectively. The other parameters are the same as those of the previous sections. Fig. 4.7(a)-(c) show the dispersion curves, the group index, and the leakage loss of the slot waveguides composed of 1-D PC cavity with $m = 4$, 5, and 6, respectively, where β is the propagation constant along the propagation direction, n_g is the group index. The group index at the frequency which achieves zero group velocity dispersion gets larger as the m-value increases. This is because the strength of the coupling between the neighboring resonators becomes weak as the one-period length becomes large. The group index at the frequency which achieves zero group velocity dispersion is 3.8, 4.4, and 5.3 for $m = 4$, 5, and 6, respectively. The leakage loss at the frequency that achieves zero group velocity dispersion gets smaller as the m-value increases. This is because the structure with the large m-value can change the air-hole radius gradually at the edge of the 1-D PC cavity. The nonlinear characteristics of the slot waveguides composed of 1-D PC cavity with $m = 4$, 5, and 6 is evaluated on the basis of the nonlinear coefficient. The effective mode area, the group index, the square of slowdown factor, and the nonlinear

coefficient are summarized in Table 4.2. The effective mode area gets smaller as the *m*-value becomes large. Furthermore, the group index gets larger as the *m*-value becomes large. In consequence, the largest nonlinear coefficient can be obtained for $m = 6$. Therefore, the nonlinear coefficient can be enlarged by increasing the *m*-value. However, the nonlinear coefficient depends strongly on wavelength in large *m*-value as shown in Fig. 4.8, which shows the wavelength dependence of the nonlinear coefficient of the slot waveguide composed of 1-D PC cavity. There is the trade-off between the nonlinear coefficient and the bandwidth. If the overlarge *m*-value is set to enlarge the nonlinear coefficient, the bandwidth becomes extremely narrow. Moreover, in this case, the one-period length of slot waveguide composed of 1-D PC cavity becomes large. Therefore, the *m*-value have to be chosen carefully in terms of the operation bandwidth and the device size.

Finally, the nonlinear characteristics are compared with the other designs of the nonlinear optical waveguides, namely the slot waveguides with nonlinear material and the Si engineered PC waveguides, as shown in Table 4.3. Note that the results of the other designs of the nonlinear optical waveguides are experimentally measured results. The slot waveguide composed of 1-D PC cavity is expected to be a good candidate for the enhancement of the nonlinear optical effects.

4.6 Conclusion

The nonlinear characteristics of the slot waveguide composed of 1-D PC cavity is investigated by evaluating its nonlinear coefficient. The numerical results have shown that the maximum nonlinear coefficient of 11 600 $m^{-1}W^{-1}$ is obtained in the optimized structure with width and height of $w = h =$ 300 nm. The maximum nonlinear coefficient is not obtained in the structure that achieves the smallest effective mode area or the largest group index. Therefore, the optimum parameters have to be explored for the enhancement of the optical nonlinear effects. Also, there is the trade-off between the nonlinear coefficient and the bandwidth in structure with different number of holes. The nonlinear coefficients can be enlarged by increasing the *m*-value. However, the bandwidth becomes extremely narrow if the overlarge *m*-value is set. Therefore, the *m*-value has to be chosen carefully in terms of the operation bandwidth and the nonlinear coefficient.

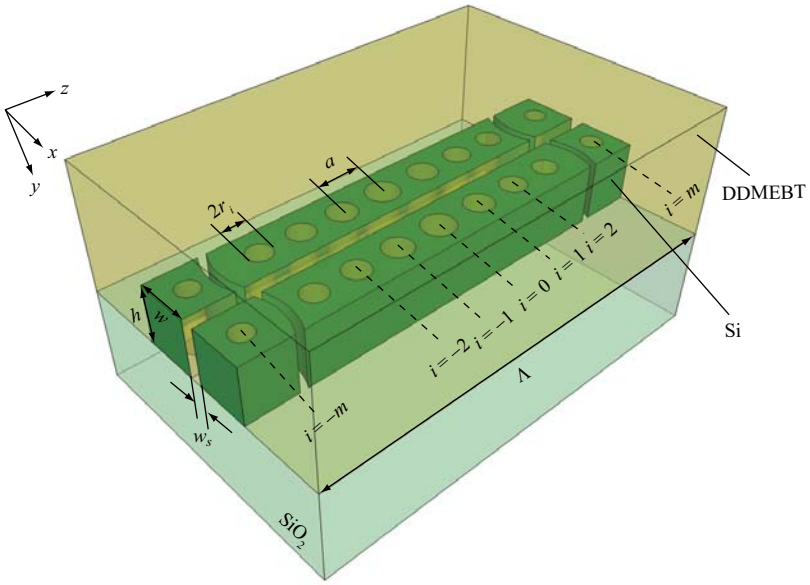

Fig. 4.1 Schematic of slot waveguide composed of 1-D PC cavity.

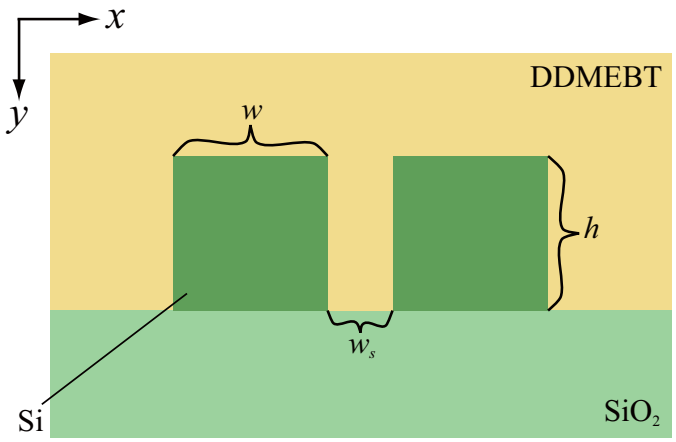

Fig. 4.2 Crosssection of slot waveguide.

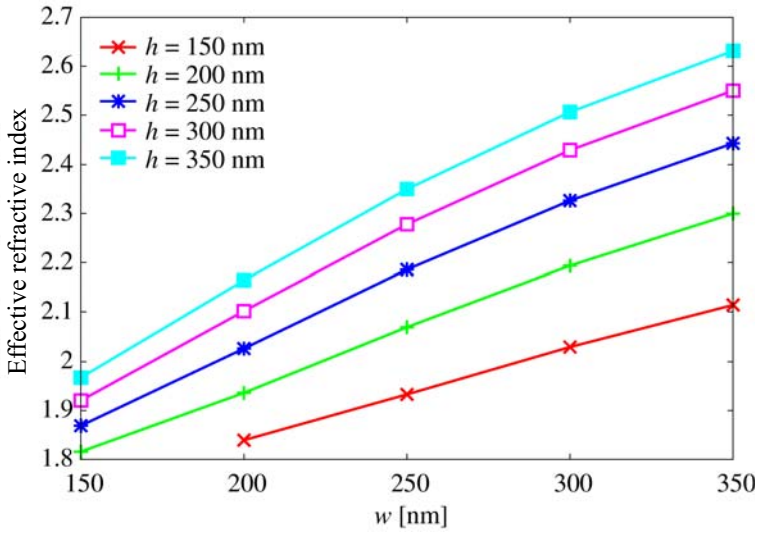

(a)

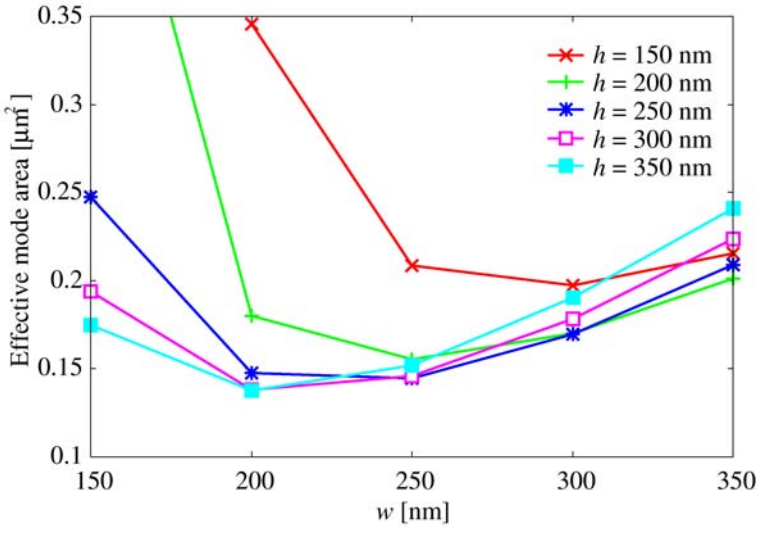

(b)

Fig. 4.3 Structural dependence of (a) effective refractive index and (b) effective mode area.

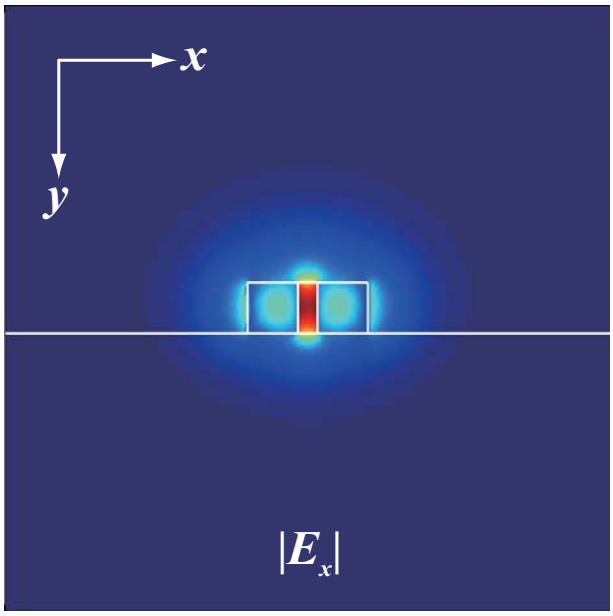

(a)

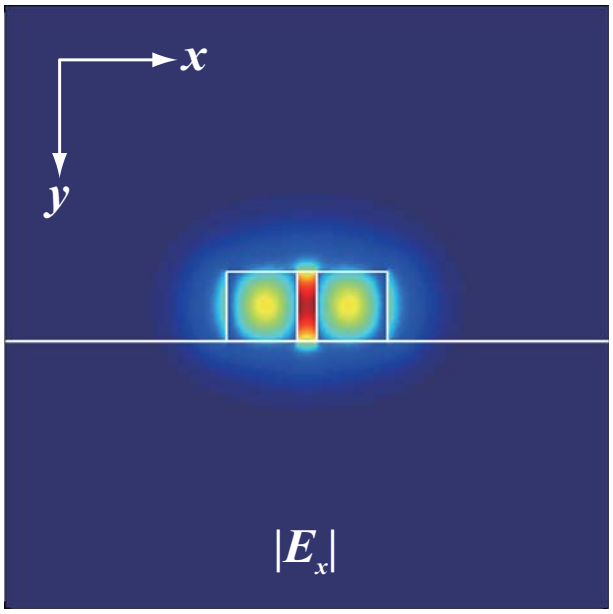

(b)

Fig. 4.4 Electromagnetic field distribution of the slot waveguide with (a) $w = h = 250$ nm and (b) $w = h = 350$ nm.

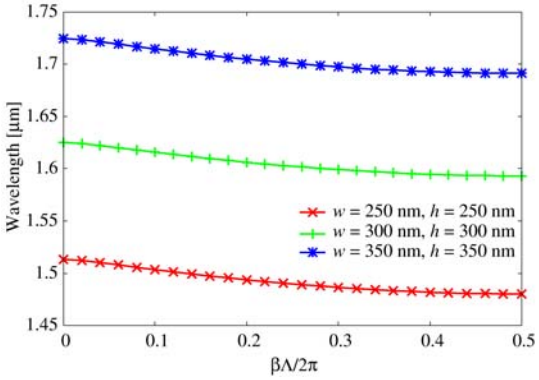

(a)

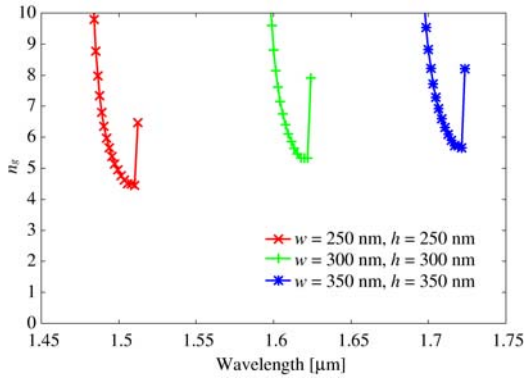

(b)

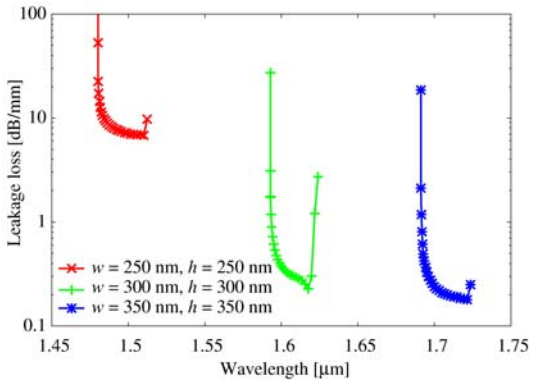

(c)

Fig. 4.5 (a) Dispersion curves, (b) group index, and (c) leakage loss of slot waveguide composed of 1-D PC cavity with different *w* and *h*.

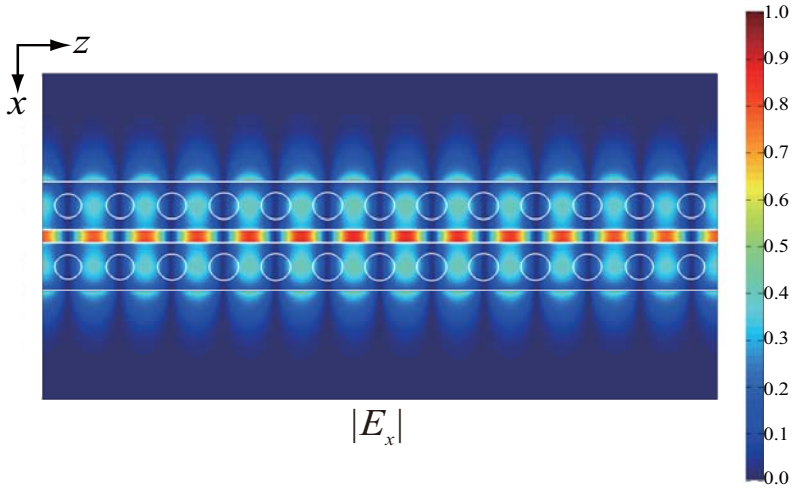

Fig. 4.6 Electromagnetic field distribution of
slot waveguide composed of 1-D PC cavity (one-period).

Table 4.1. Effective mode area, group index, square of slowdown factor, and nonlinear coefficient of slot waveguide composed of 1-D PC nanobeam cavity with different w and h.

w, h [nm, nm]	250, 250	300, 300	350, 350
A_{eff} [μm^2]	4.24×10^{-2}	4.97×10^{-2}	6.15×10^{-2}
n_g	4.4	5.3	5.6
S^2	6.11	8.76	9.86
γ_{eff} [$m^{-1}W^{-1}$]	10200	11600	9900

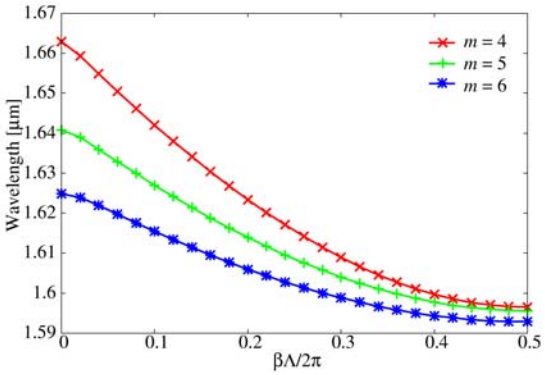

(a)

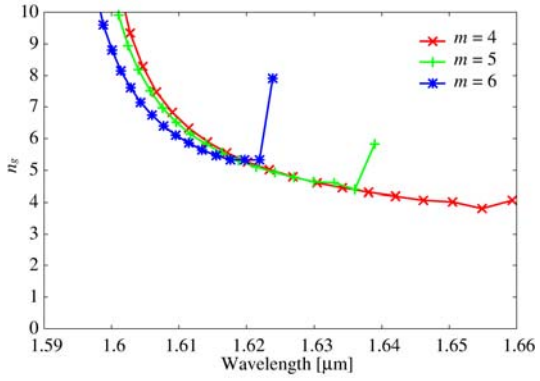

(b)

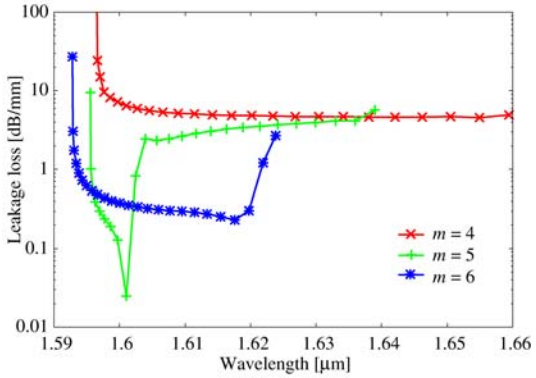

(c)

Fig. 4.7 (a) Dispersion curves, (b) group index, and (c) leakage loss of slot waveguide composed of 1-D PC cavity with different *m*-value.

Table 4.2. Effective mode area, group index, square of the slowdown factor, and nonlinear coefficient of slot waveguide composed of 1-D PC cavity with different *m*-value.

m	4	5	6
A_{eff} [μm^2]	7.40×10^{-2}	6.18×10^{-2}	4.25×10^{-2}
n_g	3.8	4.4	5.3
S^2	4.48	5.98	8.76
γ_{eff} [m^{-1}W^{-1}]	3900	6300	11600

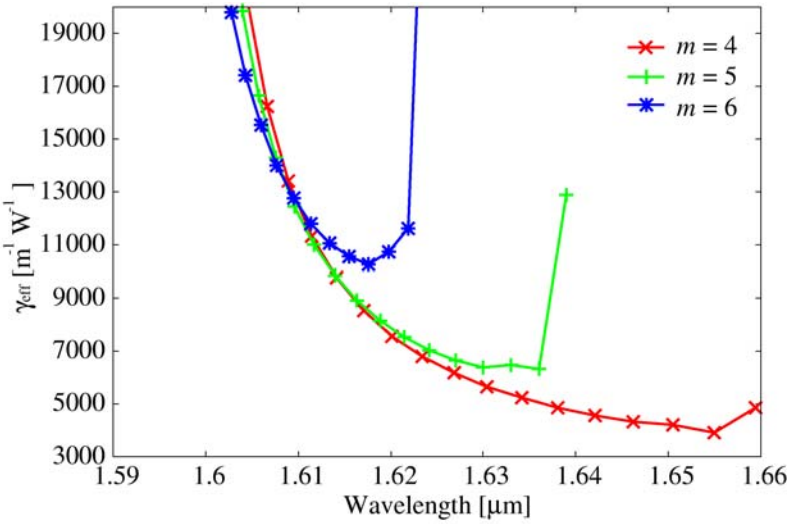

Fig. 4.8 Wavelength dependence of nonlinear coefficient.

Table 4.3 The comparison of nonlinear characteristics between the other designs of the nonlinear optical waveguides and the our proposed strucutre.

		A_{eff} [μm^2]	S^2	n_2 [m^{2}W^{-1}]	γ_{eff} [m^{-1}W^{-1}]
Slot waveguides with nonlinear material	[45]	< 0.1	N/A	1.7×10^{-17}	~ 100
	[41]	0.105	N/A	2.2×10^{-16}	6950
Si engineered PCWs	[5]	0.3	72	5.0×10^{-18}	4960
	[7]	0.3	130	5.0×10^{-18}	8800
Slot waveguide composed of PC nanobeam cavities with optimized parameters		0.0425	8.76	1.7×10^{-17}	11600

Chapter 5 Nonlinear characteristics of coupled resonator optical waveguide based on slotted one-dimensional photonic crystal cavity

5.1 Introduction

Nonlinear optical effects play a key role in the all-optical signal processing for the future photonic network. The slow-light waveguides can enhance the interaction between the light and the matter [1, 2] and the slow-light-enhanced self phase modulation (SPM) [7, 8] and four wave mixing (FWM) [13] have been reported. A photonic crystal coupled resonator optical waveguide (PC-CROW) [28], which is composed of cascaded PC cavities along the propagation direction, is highly attractive for the enhancement of the optical nonlinear effects because of its small group velocity and zero group velocity dispersion at the center of the transmission band [12]. The propagation characteristic of the PC-CROW is governed by a selection of the cascaded PC cavities. Recently, 1-D and 2-D PC cavities with a slot configuration were reported [51-55]. The electromagnetic field is strongly localized in the narrow and low-index slot region and the small effective area can be obtained like conventional slot waveguides [38]. As a result, the interaction between the light and the matter can be enhanced. In addition, filling the slot region with a material that has a large nonlinear index, further enhancement of the optical nonlinearity can be expected [44-46]. However, the PC-CROW based on such slotted PC cavity has not been reported yet.

In this chapter, a CROW based on a slotted 1-D PC cavity is proposed to enhance the optical nonlinear effects. The 1-D PC cavity has the advantages in terms of the structural simplicity and the compactness compared with the 2-D PC counterpart. The optical nonlinearity is investigated using the 3-D vector FEM for the periodic waveguide analysis [78, 80]. Numerical results show that a large nonlinear parameter exceeding 10^4 $m^{-1}W^{-1}$ can be obtained because of the slow-light effect of the CROW and the small effective area of the slotted 1-D PC cavity.

5.2 Schematic of CROW based on slotted 1-D PC cavity

Fig. 5.1 shows a schematic of a slotted 1-D PC cavity. The arrays of the holes are introduced into a silicon wire waveguide to compose the bragg mirror of the 1-D PC cavity. The slot region is located at the center of the 1-D PC cavity and its edge shape is circular. The circular-shape slot edge can be connected with the array of the holes smoothly compared with the rectangular-shape one because the circular edge can be interpreted as the inscribed holes at the end of the slot region. The core, under-

cladding, and over-cladding materials are assumed as Si ($n_{Si} = 3.5$), SiO_2 ($n_{SiO2} = 1.45$), and DDMEBT [81] ($n_{DDMEBT} = 1.8$). Since the DDMEBT has a low index than Si and a large nonlinear index $n_2 = 1.7\times10^{-17}$ m^2W^{-1}, which is three times larger than that of Si, it is suitable for the over-cladding material of the slotted 1-D PC cavity. In addition, the slot region and the holes can be homogenously filled with DDMEBT in practice because of its molecule structure [81]. The waveguide parameters are set as follows; The lattice constant a = 400 nm, the waveguide width w = 540 nm, the waveguide height h = 200 nm, the slot width w_s = 100 nm, the one cavity length is Λ, and the slot length is L. All the holes are numbered from the vicinity of the slot region to the edge of the 1-D PC cavity as shown in Fig. 5.1. The number of the one-sided holes is set as m = 5, 6, and 7. The hole radius gradually increases to suppress the mode mismatch between the slot region and the bragg mirror. The maximum hole radius is limited to 100 nm, therefore, each hole radius is set as r_1 = 60 nm, r_2 = 70 nm, r_3 = 80 nm, r_4 = 90 nm, and $r_5 = r_6 = r_7$ = 100 nm. Finally, the CROW is composed by cascading such slotted 1-D PC cavity along the propagation direction (z direction in Fig. 5.1).

5.3 Nonlinear characteristics of CROW based on slotted 1-D PC cavity

The 3-D vector FEM for periodic waveguide analysis [78, 80] is applied to the CROW based on the slotted 1-D PC cavity. Fig. 5.2 shows the dispersion curves for m = 5, 6, and 7 when the slot length L changes from 0.85 to 0.95 μm. The range of the slot length is set to excite a third order cavity mode, which presents a good balance between a quality factor and a mode volume [55]. It can be seen that the dispersion curves have a sinusoidal form, which is the characteristics of the dispersion curves of the CROW. The zero group velocity dispersion is obtained at the center of the transmission band where the slope is constant. Fig. 5.3 shows the slot length dependence of the normalized group velocity v_g/c as a function of the wavelength, where v_g is the group velocity and c is the velocity of light in vacuum. It can be seen that the normalized group velocity decreases as the slot length is long. The group velocity of the CROW is governed by the strength of the coupling between the cascaded cavities. Fig. 5.4(a) and (b) show the electric field distribution in the xz cross section of L = 0.85 μm (m = 5) and L = 0.95 μm (m = 5), respectively. Since the light confinement into the slot region of L = 0.95 μm is stronger than that of L = 0.85 μm, the coupling between the cascaded cavities is weak. As a result, the normalized group velocity is small for the long slot length. Also, the normalized group velocity decreases as the m-value is large. Fig. 5.4(b) and (c) show the electric field distribution in the xz cross section of m = 5 (L = 0.95 μm) and m = 7 (L = 0.95 μm), respectively. In the large m structure, since the electric field distribution at the edge of the slotted 1-D PC cavity is weak, the coupling between cascaded cavities is weak. As a result, the normalized group velocity is small for the large m. Fig. 5.5 shows the slot length dependence of the nonlinear parameter γ as a function of the wavelength for m = 5, 6, and 7. The nonlinear parameter is calculated by the following rigorous definition reported recently [83];

$$\gamma = \frac{k_0 n_2}{A_{\text{eff}}}. \tag{5.1}$$

$$A_{\text{eff}} = \frac{1}{\Lambda}\frac{\mu_0}{\varepsilon_0}\frac{\left|\int_z^{z+\Lambda}\int_{-\infty}^{\infty}\int_{-\infty}^{\infty}\text{Re}\left[\boldsymbol{e}\times\boldsymbol{h}^*\right]\cdot\boldsymbol{i}_z\,dxdydz\right|^2}{\int_z^{z+\Lambda}\iint n_0^2\left|\boldsymbol{e}\right|^4 dxdydz}, \tag{5.2}$$

where k_0 is the wavenumber in vacuum, A_{eff} is the effective area especially defined for periodic waveguides [83], Λ is the one cavity length, ε_0 and μ_0 are the permittivity and permeability in vacuum, $\boldsymbol{e}$ and $\boldsymbol{h}$ are the electric and magnetic field vectors, n_2 is the nonlinear index, n_0 is the refractive index. The nonlinear parameter scales with the square of the slowdown factor S defined as v_φ/v_g [2], where v_φ is the phase velocity. Therefore, the large nonlinear parameter is obtained in the structure with long slot length. However, too long slot length is not preferable because of the leakage loss discussed below. Fig. 5.6 shows the slot length dependence of the leakage loss as a function of the wavelength for m = 5, 6, and 7. The leakage loss is calculated as

$$Leakage\ loss = 20\log_{10} e \times \left|\text{Im}\left(\beta\right)\right|, \tag{5.3}$$

where Im(β) is the imaginary part of the propagation constant, which is given by

$$\text{Im}\left(\beta\right) = \frac{\text{Im}\left(\omega\right)}{v_g}, \tag{5.4}$$

where Im(ω) is the imaginary part of the angular frequency [79]. The leakage loss depends on the slot length and the minimum value is obtained for L = 0.9 μm in all m-value structures. We consider that the envelope curves of the electromagnetic field distribution close in the Gaussian function changing the slot length. Therefore, too much increase of the slot length is not suitable approach to decrease the group velocity for the enhancement of the optical nonlinearity. In the structure with L = 0.9 μm, the nonlinear parameters of $\gamma = 3.54\times10^3$, 6.52×10^3, and 1.28×10^4 $\text{m}^{-1}\text{W}^{-1}$ are obtained for m = 5, 6, and 7 at the zero group velocity dispersion wavelength, respectively. The large nonlinear parameter is obtained in the structure with the large m. However, there is a trade-off between the nonlinear parameter and the operation bandwidth as shown in Fig. 5.5. Therefore, the number of holes has to be chosen carefully in terms of the operation bandwidth.

5.4 Slot-width dependence of nonlinear parameter

The further enhancement of the optical nonlinear effects is considered by decreasing the slot width w_s. As noted previous section, too long slot length is not preferable because of the leakage loss and there is the trade-off between the nonlinear parameter and the leakage loss. Recently, some of the slotted PC cavity with the slot width less than 100 nm is reported in experiment [51, 53]. In this section, the slot width dependence of the optical nonlinearity is investigated in the range from w_s = 40 nm to 100 nm. The slot length is fixed as L = 0.9 μm to suppress the leakage loss. The other parameters are the

same as the previous section. Fig. 5.7 shows the dispersion curves for m = 5, 6, and 7 when the slot width w_s changes. The redshift of dispersion curves is observed when the slot width decreases. When the confinement of the light in the narrow and the low-index slot region increases, the propagation constant β decreases in the same wavelength. As a result, the redshift of the dispersion curves occurs. Fig. 5.8 shows the slot width dependence of the normalized group velocity as a function of the wavelength. As the slot width decreases, the normalized group velocity becomes small. Fig. 5.9(a) and (b) show the electric field distribution at xz cross section of w_s = 100 nm and w_s = 40 nm with m = 5. The light confinement into the slot region of w_s = 40 nm is stronger than that of w_s = 100 nm. The narrow slot width makes the light localization at the center of the cavity strong, then, the strength of coupling between the cascaded cavities becomes weak. As a result, the group velocity decreases in the structure with the narrower slot width. Fig. 5.10 shows the slot width dependence of the nonlinear parameters for m = 5, 6, and 7. The nonlinear parameter is inversely proportional to the slot width since the small effective mode area is provided by the narrow slot region and the nonlinear parameter inversely scales with the effective area as shown in Eq.(5.1). In the structure with w_s = 40 nm, the nonlinear parameters of $\gamma = 8.71\times10^3$, 1.14×10^4, and 1.63×10^4 $\mathrm{m^{-1}W^{-1}}$ are obtained for m = 5, 6, and 7 at the zero group velocity dispersion wavelength, respectively. These nonlinear parameters are approximately 10^2 times larger than that of conventional silicon wire waveguides. Fig. 5.11 shows the slot width dependence of the leakage loss as a function of the wavelength. It can be seen that the leakage loss decreases with narrower slot width. The structure of narrow slot width has advantages in terms of both the leakage loss and the nonlinear parameter. In general, there are the leakage loss, the waveguide dependent loss, and the insertion loss in the losses of optical waveguides. To estimate the optimum number of cavities of CROW, the balance between the leakage loss and the nonlinear parameter is the important criteria. Fig. 5.12 shows the relationship between the nonlinear parameter and the effective length L_{eff}. The effective length is the nonlinear interaction length considering the leakage loss and calculated as

$$L_{\mathrm{eff}} = \frac{1 - e^{-\alpha L_{\mathrm{phys}}}}{\alpha}, \tag{5.5}$$

where α is the attenuation constant and the L_{phys} is the physical length, which is fixed as 100 μm and $10 \times \Lambda$ for comparison. The color and the type of points in Fig. 5.12 represent the number of holes and the slot width, respectively. The performance increases as the points are plotted at the upper right side. It can be seen that the structure of m = 7 and w_s = 0.04 μm is the appropriate parameter of the CROW based on slotted 1-D PC cavity in terms of the trade-off between the nonlinear parameter and the effective length, while the consideration of the bandwidth is needed. Considering the nonlinear conversion such as the four wave mixing, since the bandwidth narrows in proportion of the increase of the nonlinear parameter, the proposed CROW with the extremely large m-value is not preferable.

5.5 Conclusion

The coupled resonator optical waveguide based on the slotted 1-D PC cavity was proposed and its enhancement of the optical nonlinearity due to the slow-light effect of the CROW and the small effective area of the slotted 1-D PC cavity has been investigated. Using the 3-D vector FEM for the periodic waveguides analysis, the trade-off between the nonlinear parameter and the leakage loss was found. Additionally, to enhance the optical nonlinear effects further, the structure with narrow slot width was investigated and its advantages in terms of both the leakage loss and the nonlinear parameter were demonstrated. Setting the slot length and width appropriately, the largest nonlinear parameter 1.63×10^{4} $m^{-1}W^{-1}$ of the CROW based on the slotted 1-D PC cavity can be obtained.

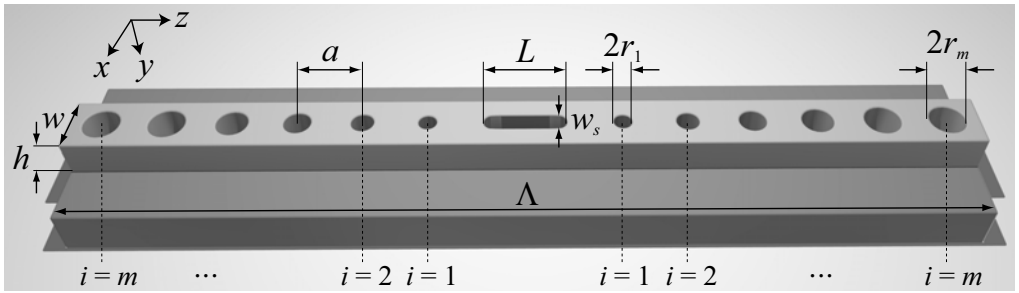

Fig. 5.1 A schematic of a slotted 1-D PC cavity.

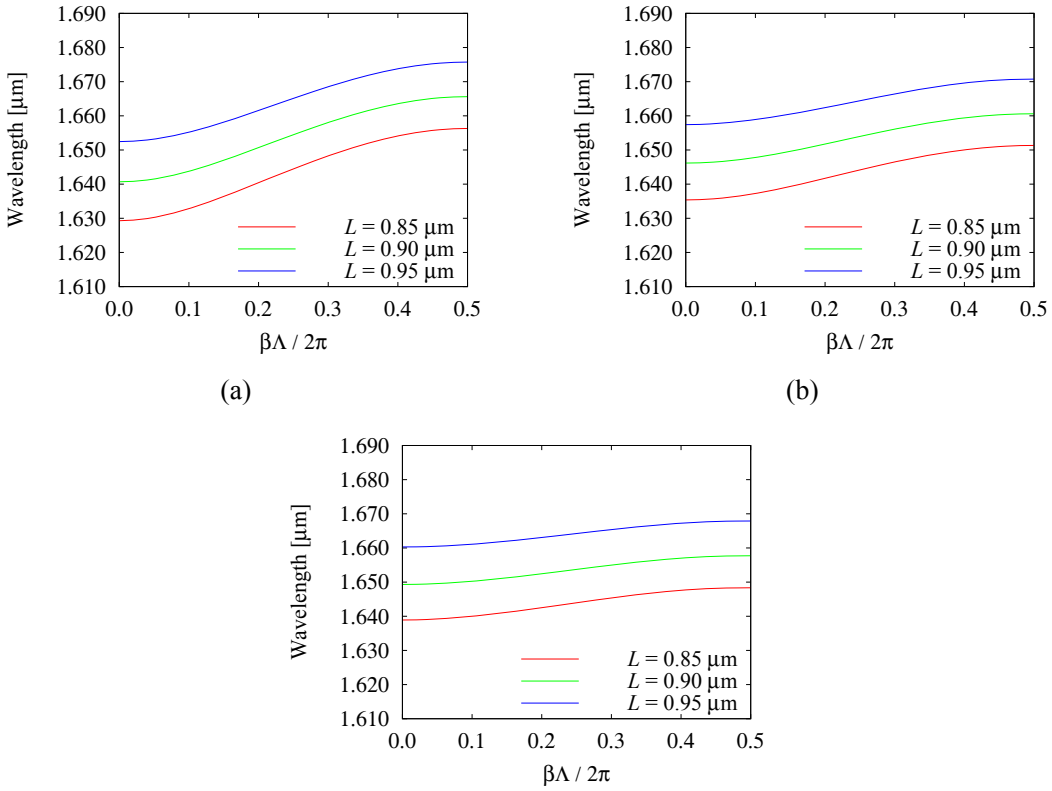

Fig. 5.2 The slot length dependence of the dispersion curves for (a) $m = 5$, (b) $m = 6$, and (c) $m = 7$.

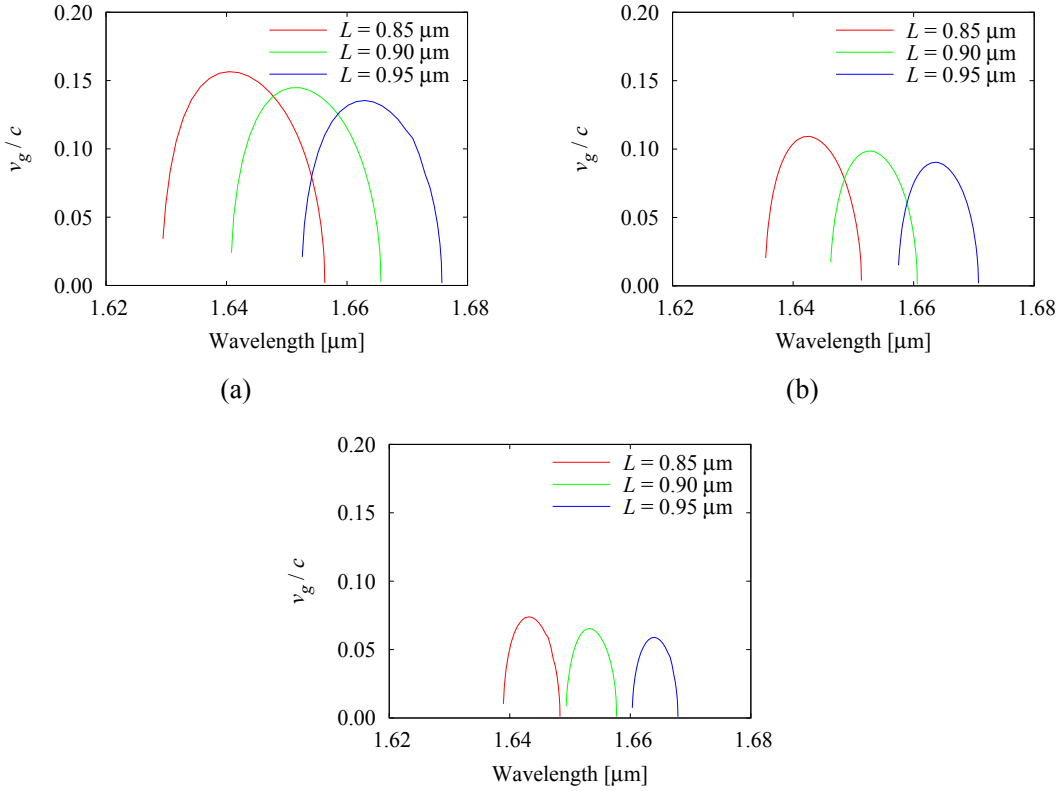

(a) (b)

(c)

Fig. 5.3 The slot length dependence of the normalized group velocity for (a) m = 5, (b) m = 6, and (c) m = 7.

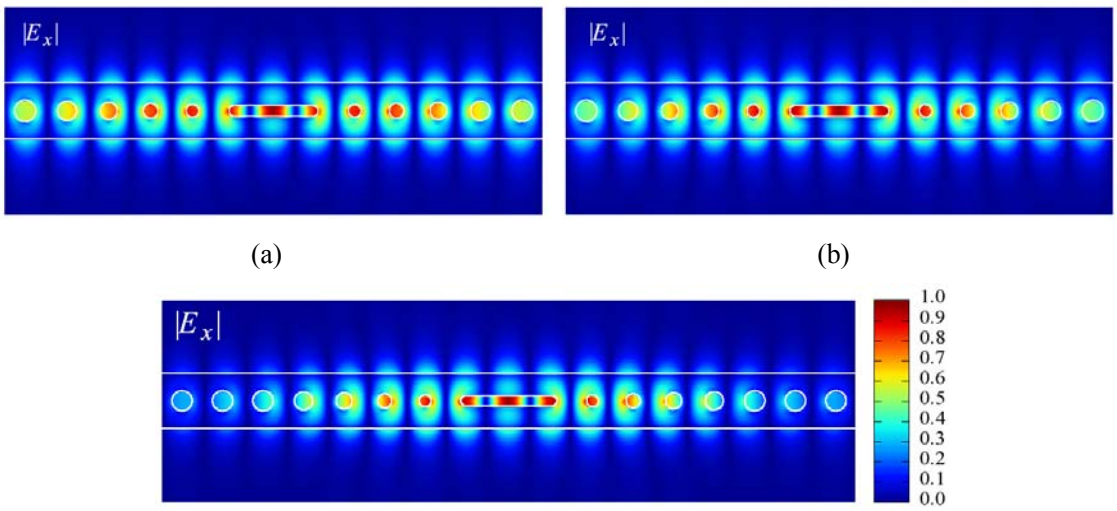

(a) (b)

(c)

Fig. 5.4 The electric field distribution of (a) m = 5, L = 0.85 μm, (b) m = 5, L = 0.95 μm, and (c) m = 7, L = 0.95 μm.

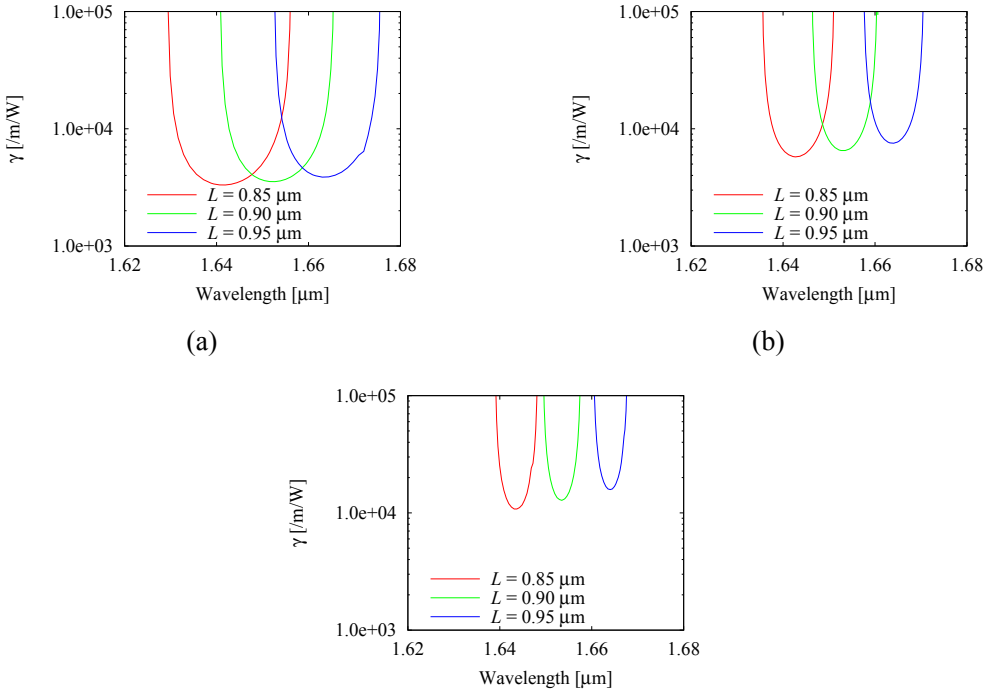

(a) (b)

(c)

Fig. 5.5 The slot length dependence of the nonlinear parameter for (a) $m = 5$, (b) $m = 6$, and (c) $m = 7$.

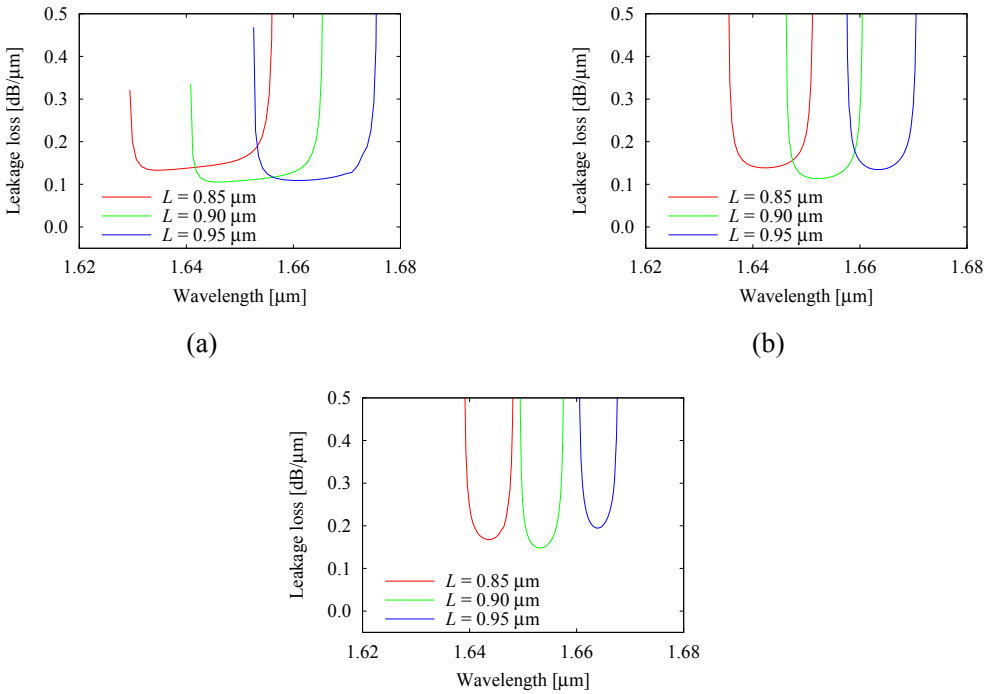

(a) (b)

(c)

Fig. 5.6 The slot length dependence of the leakage loss for (a) $m = 5$, (b) $m = 6$, and (c) $m = 7$.

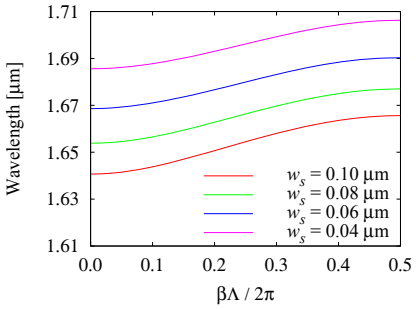

(a)

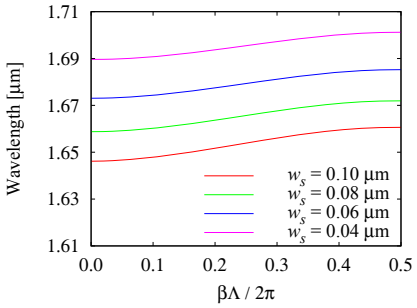

(b)

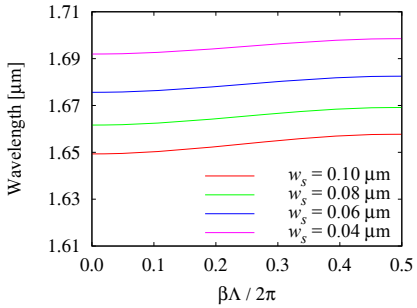

(c)

Fig. 5.7 The slot width dependence of the dispersion curves for (a) m = 5, (b) m = 6, and (c) m = 7.

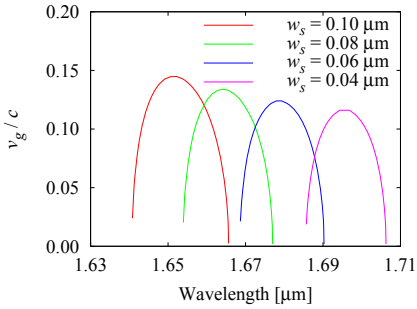

(a)

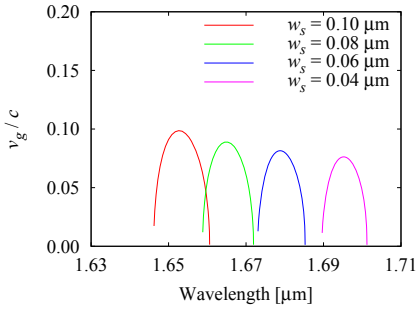

(b)

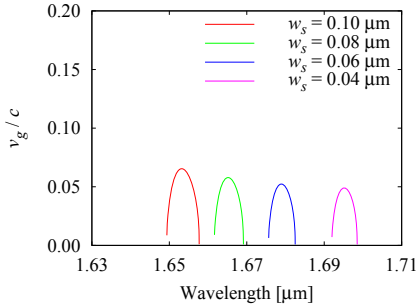

(c)

Fig. 5.8 The slot width dependence of the group velocity for (a) m = 5, (b) m = 6, and (c) m = 7.

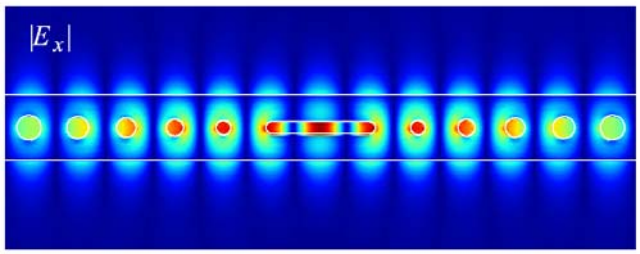

(a)

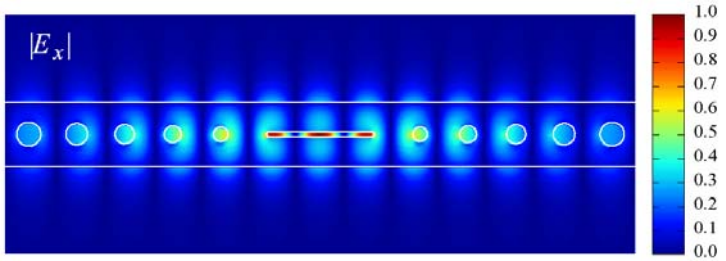

(b)

Fig. 5.9 The electric field distribution for (a) w_s = 100 nm and (b) w_s = 40 nm, where m = 5, L = 0.9 μm.

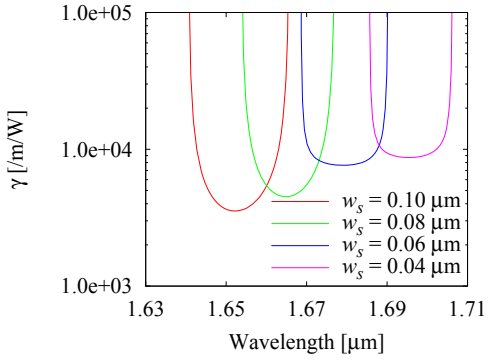

(a)

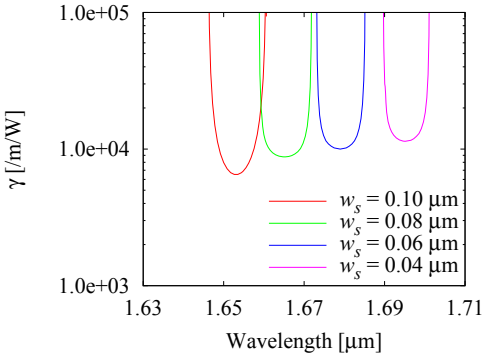

(b)

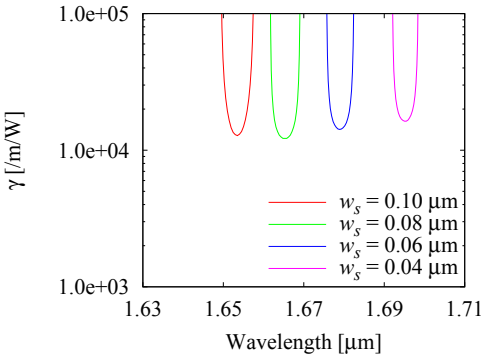

(c)

Fig. 5.10 The slot width dependence of the nonlinear parameter for (a) m = 5, (b) m = 6, and (c) m = 7.

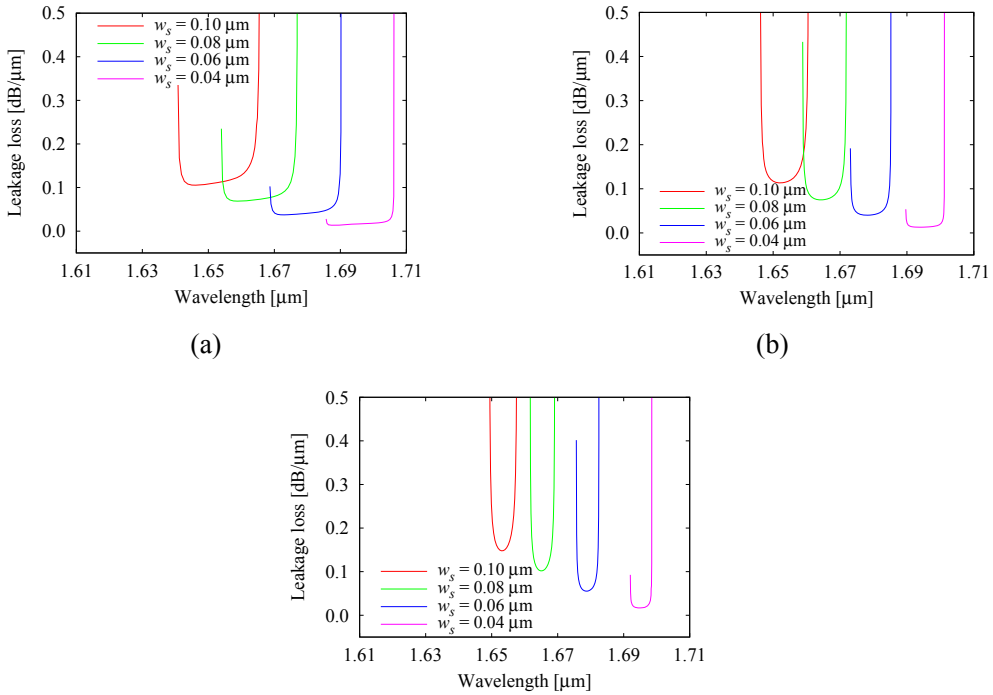

Fig. 5.11 The slot width dependence of the leakage loss for (a) m = 5, (b) m = 6, and (c) m = 7.

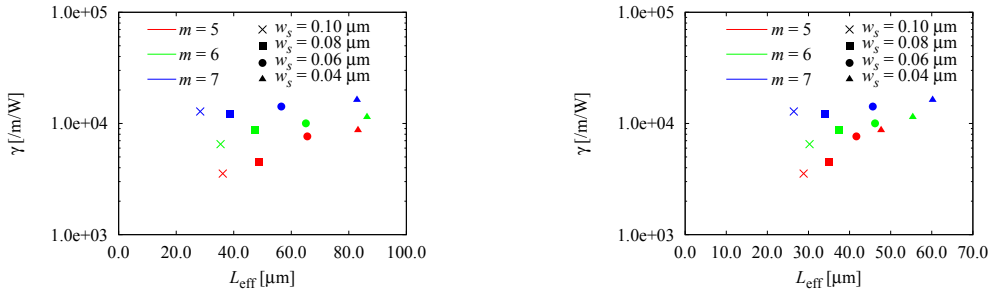

Fig. 5.12 The relationship between the nonlinear parameter and effective length for (a) L_{phy} = 100 μm and (b) L_{phy} = 10 × Λ.

Chapter 6 Three-dimensional analysis of taper waveguide for highly-efficient connection between coupled resonator optical waveguide and straight waveguide

6.1 Introduction

If the CROW structures are introduced to the optical circuits in practice, the optical pulse is launched from the straight waveguide. The taper waveguide is the essential component to realize the highly-efficient connection with the input waveguide over the wide bandwidth. Although a taper waveguide aiming for a highly-efficient connection is evaluated by 2-D analysis [76], 3-D analysis has not been reported yet. The 3-D analysis is necessary for the consideration of the radiation to the vertical direction. The 3-D analysis of the taper waveguide is carried out, for the first time, using the newly developed 3-D FETD-BPM. The developed 3-D FETD-BPM is the powerful tool to design the optical waveguide in practice because it can evaluate the reaction of the optical pulse. The highly-efficient connection between the straight waveguide and the CROW structures over the wide bandwidth is demonstrated.

6.2 Formulation of 3-D FETD-BPM

A 3-D optical waveguide surrounded by the PML regions with the thickness d_i (i = 1, 2, 3) is considered as shown in Fig. 6.1. With these assumptions and Maxwell's equation, the following vector wave equation can be obtained:

$$\nabla \times \left(\left[p \right] \nabla \times \boldsymbol{\Phi} \right) + \frac{\left[q \right]}{c^2} \frac{\partial^2 \boldsymbol{\Phi}}{\partial t^2} = \mathbf{0}, \tag{6.1}$$

$$\left[p \right] = \left[\mu_r \right]_{PML}^{-1}, \left[q \right] = \left[\varepsilon_r \right]_{PML}, \text{ for } \boldsymbol{\Phi} = \boldsymbol{E}, \tag{6.2}$$

$$\left[p \right] = \left[\varepsilon_r \right]_{PML}^{-1}, \left[q \right] = \left[\mu_r \right]_{PML}, \text{ for } \boldsymbol{\Phi} = \boldsymbol{H}, \tag{6.3}$$

where $\boldsymbol{E}$ and $\boldsymbol{H}$ are the electric and magnetic vector fileds, c is the velocity of light in vacuum, and $\mathbf{0}$ is null vector. In 3-D FETD-BPM, either the electric fields (E_x, E_y, and E_z) or the magnetic fields (H_x, H_y, and H_z) are treated, and the electric field is calculated in this paper. Tensors $[\varepsilon_r]_{PML}$ and $[\mu_r]_{PML}$ are the relative permittivity and permeability considering the PML and written as

$$\left[\varepsilon_r \right]_{PML} = n^2 \left[\Lambda \right], \tag{6.4}$$

$$\left[\mu_r \right]_{PML} = \left[\Lambda \right], \tag{6.5}$$

$$[\Lambda] = \begin{bmatrix} \frac{s_y s_z}{s_x} & 0 & 0 \\ 0 & \frac{s_z s_x}{s_y} & 0 \\ 0 & 0 & \frac{s_x s_y}{s_z} \end{bmatrix}, \tag{6.6}$$

where n is the refractive index, and s_x, s_y, and s_z are given in Table 6.1. The values of s_i (i = 1, 2, 3) in Table 6.1 are taken as

$$s_i = 1 - j\left(\frac{\rho}{d_i}\right)^2 \tan\delta_i, \tag{6.7}$$

where d_i (i = 1, 2, 3) is the thickness of the PML along the x, y, and z directions, ρ is the distance from the beginning of the PML surface, and δ_i is the loss angle at the end of the PML ($\rho = d_i$). Note that the tensors $[\varepsilon_r]_{PML}$ and $[\mu_r]_{PML}$ in interior region (i.e. no PML region) become the scalar relative permittivity ε_r and permeability μ_r.

Using the slowly varying envelope approximation (SVEA), a slowly varying complex amplitude $\boldsymbol{\varphi}$, and a carrier center angular frequency ω_0, the following form of the solution is obtained:

$$\boldsymbol{\Phi}(x, y, z, t) = \boldsymbol{\varphi}(x, y, z)\exp(j\omega_0 t). \tag{6.8}$$

Substituting (6.8) into (6.1), we obtain the following equation:

$$\nabla \times \left([p]\nabla \times \boldsymbol{\varphi}\right) + \frac{[q]}{c^2}\left(\frac{\partial^2 \boldsymbol{\varphi}}{\partial t^2} + j2\omega_0 \frac{\partial \boldsymbol{\varphi}}{\partial t} - \omega_0^2 \boldsymbol{\varphi}\right) = \mathbf{0}. \tag{6.9}$$

An analysis domain Ω is divided into the constant tangential and linear normal (CT/LN) tetrahedral edge elements. The field $\boldsymbol{\varphi}$ can be approximated as

$$\boldsymbol{\varphi}(x, y, z) = \{N\}^T \{\phi\}_e \tag{6.10}$$

where $\{N\}$ is the shape function vector, $\{\phi\}_e$ is the edge variables for each element, and superscript T denotes a transpose. Applying the standard finite-element technique to (6.9), we obtain

$$\frac{1}{c^2}[M]\frac{\partial^2 \{\phi\}}{\partial t^2} + j2\frac{\omega_0}{c^2}[M]\frac{\partial \{\phi\}}{\partial t} + \left([K] - \frac{\omega_0^2}{c^2}[M]\right)\{\phi\} = \mathbf{0}, \tag{6.11}$$

where $\{\phi\}$ is all the edge variables in the analysis domain Ω. The finite-element matrices are given by

$$[K] = \sum_e \iiint_e \left(\nabla \times \{N\}\right)\left([p]\nabla \times \{N\}^T\right) d\Omega, \tag{6.12}$$

$$[M] = \sum_e \iiint_e [q]\{N\}\{N\}^T d\Omega, \tag{6.13}$$

where Σ_e denotes the summation over all different elements. Utilizing the Padé recurrence relation [84], the following approximation of a partial differential operator with respect to the time t is obtained:

$$\frac{\partial}{\partial t} \approx -\frac{c^2}{j2\omega_0}\left[M\right]^{-1}\left(\left[K\right]-\frac{\omega_0^2}{c^2}\left[M\right]\right) \tag{6.14}$$

Replacing the $\partial / \partial t$ of the first member of (6.11) with (6.14), the following equation of the 3-D FETD-BPM, which can treat wide-band optical pulses, is obtained:

$$j2\frac{\omega_0}{c^2}\left[\tilde{M}\right]\frac{\partial\left\{\phi\right\}}{\partial t}+\left(\left[K\right]-\frac{\omega_0^2}{c^2}\left[M\right]\right)\left\{\phi\right\}=\mathbf{0} \tag{6.15}$$

with

$$\left[\tilde{M}\right]=\left[M\right]+\frac{1}{4\omega_0^2}\left(\left[K\right]-\omega_0^2\left[M\right]\right). \tag{6.16}$$

Applying the Crank-Nicholson algorithm for the time t to (6.15) yields

$$\left[A\right]_i\left\{\phi\right\}_{i+1}=\left[B\right]_i\left\{\phi\right\}_i, \tag{6.17}$$

$$\left[A\right]_i=-j2\frac{\omega_0}{c^2}\left[\tilde{M}\right]+0.5\Delta t\left(\left[K\right]-\frac{\omega_0^2}{c^2}\left[M\right]\right), \tag{6.18}$$

$$\left[B\right]_i=-j2\frac{\omega_0}{c^2}\left[\tilde{M}\right]-0.5\Delta t\left(\left[K\right]-\frac{\omega_0^2}{c^2}\left[M\right]\right), \tag{6.19}$$

where Δt is a time step size, $\{\phi\}_i$ and $\{\phi\}_{i+1}$ is all the edge variables at the i-th and (i+1)-th time step. Once an initial field $\{\phi\}_0$ is set, the time-varying field propagation is calculated by the sequential computation. The initial field with an eigen mode of waveguides in the transverse direction and a Gaussian profile in the longitudinal direction at $t = 0$ are taken as

$$\boldsymbol{\varphi}\left(x,y,z\right)=\boldsymbol{\varphi}_0\left(x,y\right)\exp\left[-\left(\frac{z-z_0}{2\sigma^2}\right)^2\right]\exp\left[-j\beta\left(z-z_0\right)\right], \tag{6.20}$$

where $\boldsymbol{\varphi}_0$ is the electromagnetic field distribution at the cross section of waveguides, β is the propagation constant, z_0 is the center position of the input pulse, and σ is the standard deviation of the Gaussian function. Fig. 6.2 shows the electric field distribution of a propagating optical pulse at the xz cross section in a silicon wire waveguide. The white line represents a boundary between the core and the cladding. In 3-D FETD-BPM simulation, the input pulse is given in the input port located away from the analysis components. The launched pulse propagates toward the output port, and then, the transmitted pulse is monitored at output port every time steps. The fast fourier transform of the time dependence of the monitored pulse, normalized to the spectrum of the input pulse, gives the transmission spectrum. When the pulse reaches the boundary between the interior region and PML region, the absorption of the pulse occurs. Setting the PML parameters appropriately, the pulse is successfully absorbed in PML region as shown in Fig. 6.2(d).

6.3 Confirmation of validity of 3-D FETD-BPM

To confirm the validity of the presented 3-D FETD-BPM, transmission characteristics of a photonic crystal cavity as shown in Fig. 6.3 are demonstrated firstly. The periodic array of holes are introduced into a silicon wire waveguide. The photonic crystal cavity has the same parameters as [85] for comparison. The waveguide width w is 470 nm, the silicon thickness t_{Si} is 200 nm, the lattice constant a is 420 nm, the hole radius r is 100 nm, the defect length a_d is 630 nm, and the total etch depth of the silicon and SiO_2 t_{etch} is 550 nm. In the 3-D FETD-BPM simulation, the time step size Δt is set to 5 fs, which ensures a balance between numerical accuracy and computational cost. The straight waveguides without air holes are connected to each side of the photonic crystal cavity. The optical pulse is launched from one side of the straight waveguide, and the transmitted pulse is monitored at the other side every time step. Fig. 6.4 shows the transmission spectrums of the photonic crystal cavity, which are obtained by the FDTD simulation [85], the experiment [85], and the 3-D FETD-BPM. Our result is in agreement with the measured value and the numerical value using FDTD.

Secondary, the quality factor of a ring resonator as shown in Fig. 6.5 are demonstrated for further validation. The structural parameters of the ring resonator are taken from [86] for comparison. The silicon waveguide width w is 450 nm, the height h is 250 nm, the radius of the ring resonator R is 5 μm, and the spacing between the ring resonator and the straight waveguide d is 200 nm. Fig. 6.6 shows the transmission spectrum of the ring resonator. The resonance wavelength λ_c and the full-width-half-maximal (FWHM) bandwidth $\Delta\lambda$ are λ_c = 1567.9 nm and $\Delta\lambda$ = 0.186 nm, respectively. The quality factor Q, calculated as $Q = \lambda_c/\Delta\lambda$, is 8 402 while the measured value [86] is Q = 9 804 (λ_c = 1568.7 nm, $\Delta\lambda$ = 0.16 nm). As noted above, the 3-D FETD-BPM can investigate the quality factor of the ring resonator, and the validity of the 3-D FETD-BPM is shown.

6.4 Taper waveguide for highly-efficient connection between 1-D PC-CROW and straight waveguide

A taper waveguide for a highly-efficient connection between a straight waveguide and a one-dimensional photonic crystal coupled resonator optical waveguide (1-D PC-CROW) as shown in Fig. 6.7 is investigated using the developed 3-D FETD-BPM. The PC-CROW, which is composed by cascading photonic crystal cavities, can achieve the zero group velocity dispersion at the center of transmission bands. Among the 1-D to 3-D photonic crystal structures, the 1-D PC-CROW is the most attractive in terms of simplicity and integrability. In particular, the 1-D PC-CROW based on a high-Q cavity with modulated mode-gap can realize a small group velocity and a small leakage loss, simultaneously [37]. Therefore, the 1-D PC-CROW is a promising structure for nonlinear optical devices, which are key components for future optical networks. However, if the 1-D PC-CROW is directly connected to a silicon straight waveguide, it is difficult to obtain a high transmission over wide bands due to the reflection at connection interfaces. Although a taper waveguide aiming for a

highly-efficient connection is evaluated by 2-D analysis [76], 3-D analysis has not been reported yet. Since photonic crystal waveguides have radiation toward the vertical direction, it is important to analyze 3-D structures with a finite core height. In addition, a taper waveguide for the 1-D PC-CROW based on a high-Q cavity with modulated mode-gap is evaluated for the first time. The waveguide parameters are set as follows; The core, under-cladding, and over-cladding materials are Si ($n_{Si} = 3.45$), SiO_2 ($n_{SiO2} = 1.45$), and air ($n_{air} = 1.0$), respectively. The lattice constant is a = 400 nm, waveguide width is w = 540 nm, and waveguide height is h = 200 nm. The air holes are numbered as shown in Fig. 7, and the i-th ($i = -m$ to m) air-hole radius r_i is determined as [33]:

$$r_i = r_0 \left\{ 1 - \left(\frac{i}{M_r} \right)^2 \right\}, \tag{6.21}$$

where r_0 is the center-hole radius, M_r is the changing ratio of hole radii. If the calculated r_i is less than a given minimum hole radius r_{min}, the r_i is replaced with the r_{min}. From the previous result [37], the center-hole radius and the minimum hole radius are set to $r_0 = 120$ nm and $r_{min} = 115$ nm. The changing ratio of hole radii is set to $M_r = 19$, 25, and 27 for $m = 4$, 5, and 6, respectively. One cavity has $(2m+1)$ holes and a one-period length Λ becomes $(2m+1)a$. In this paper, the m-value is changed in the range of 4 to 6 in order to evaluate transmission characteristics in terms of the m-value. Fig. 6.8 shows schematic of a taper waveguide for a highly-efficient connection between a 1-D PC-CROW and a silicon straight waveguide. The taper waveguide is composed of N periods of the fundamental structure of the 1-D PC-CROW, whose waveguide width and hole radius are gradually reduced toward the straight waveguide. The reflection can be suppressed due to the adiabatic change of structures. Each period of the taper waveguide is numbered as shown in Fig. 6.8. The waveguide width and hole radius in the j-th ($j = 1$ to N) section of the taper waveguide are determined as

$$R_{ij} = R_0 + \frac{\left(1 - R_0\right) z_{ij}}{N\Lambda}, \tag{6.22}$$

$$w_{j-1} = w_0 + \frac{\left(w - w_0\right)\left(j - 1\right)}{N}, \tag{6.23}$$

where R_{ij} is the reduction ratio of the i-th air hole in the j-th section, R_0 is the reduction ratio of the air hole at $z = 0$, z_{ij} is the z coordinate of the i-th air hole in the j-th section, w_{j-1} is the waveguide width of the j-th section, and w_0 is the waveguide width of the straight waveguide. In our simulation, each parameter is set to $N = 4$, $R_0 = 0.2$, and $w_0 = 454$ nm, which are optimized values in 2-D analysis [76]. Fig. 6.9 shows two types of the analysis domains schematically. One is the configuration in which the taper waveguide is introduced and the other is that in which the taper waveguide is not introduced. Each configuration has 5 periods of the 1-D PC-CROW and the straight waveguide for the input and output ports. The developed 3-D FETD-BPM is applied to such structures in order to evaluate the transmission characteristics. Fig. 6.10 shows the normalized frequency dependence of transmission

for the case of m = 4, 5, and 6. The transmittance at short wavelength decreases more rapidly than that at long wavelength because of the photonic band gap (PBG) represented as a shaded region of Fig. 6.10. Since the taper waveguide has the PBG at a different frequency, a red shift of the bandwidth can be seen. In the structure without the taper waveguide, the transmission oscillates owing to the Fabry-Perot resonance, and the frequency dependence of the transmission is particularly large. On the other hand, in the structure with taper waveguide, since the reflection is suppressed, the high transmission of –0.1 dB over the 260, 287, and 301 nm wide band can be obtained in m = 4, 5, and 6, respectively. By using the taper waveguides, the flat transmission spectrum can be obtained in any m-value. Fig. 6.11 shows the electric field distributions at the xz cross section in the 1-D PC-CROW (m = 4) with and without the taper waveguide. Figs. 6.11 (a) and (c) represent the electric field distributions when the optical pulses are launched, and Figs. 6.11 (b) and (d) represent when the optical pulses reach the output port. The white solid lines represent the boundary between the core and the cladding. The white dashed lines represent the interfaces among the straight waveguide, the taper waveguide, and the 1-D PC-CROW. It can be seen that the highly-efficient connection is achieved using the taper waveguide.

6.5 Conclusion

The 3-D analysis of the taper waveguide was implemented in this chapter. If the CROW structures are introduced to the optical circuits in practice, since the optical pulse is launched from the straight waveguide, the taper waveguide is the essential component to realize the highly-efficient connection. Although a taper waveguide aiming for a highly-efficient connection is evaluated by 2-D analysis, 3-D analysis has not been reported yet. The 3-D analysis is necessary for the consideration of the radiation to the vertical direction. The 3-D analysis of the taper waveguide is carried out, for the first time, using the newly developed 3-D FETD-BPM. The highly-efficient connection (> –0.1 dB) between the straight waveguide and the CROW structures over the wide bandwidth (> 200 nm) is demonstrated.

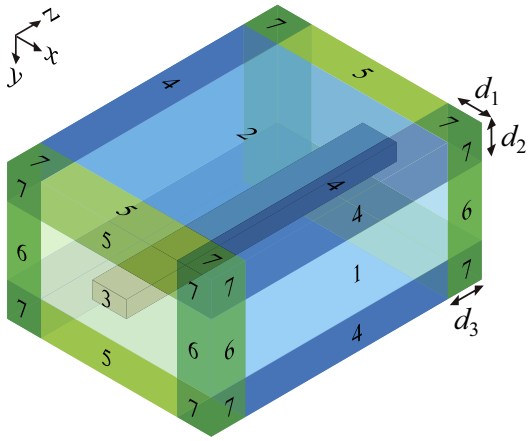

Fig. 6.1. Schematic of a 3-D optical waveguide surrounded by the PML regions.

TABLE 6.1
PML PARAMETERS

PML parameter	PML region						
	1	2	3	4	5	6	7
s_x	s_1	1	1	s_1	1	s_1	s_1
s_y	1	s_2	1	s_2	s_2	1	s_2
s_z	1	1	s_3	1	s_3	s_3	s_3

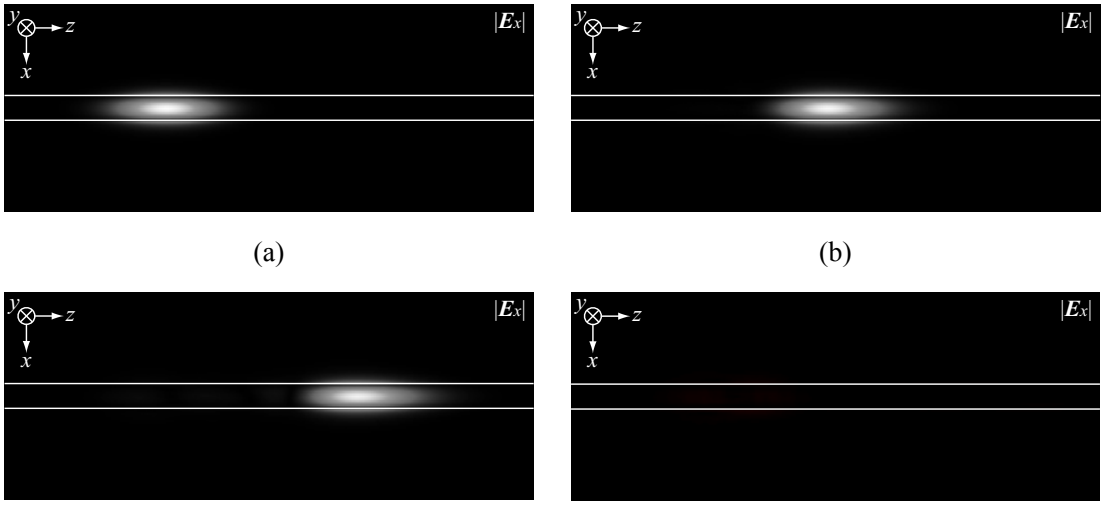

(a) (b)

(c) (d)

Fig. 6.2. The electric field distribution of a propagating optical pulse with an eigen mode of the waveguide and a Gaussian profile. (a) t = 0 fs, (b) t = 30 fs, (c) t = 60 fs, (d) t = 90 fs.

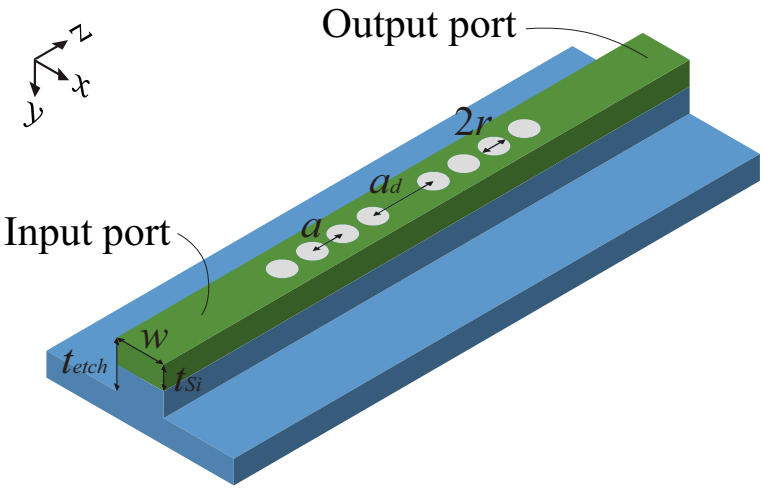

Fig. 6.3. Schematic of a photonic crystal cavity.

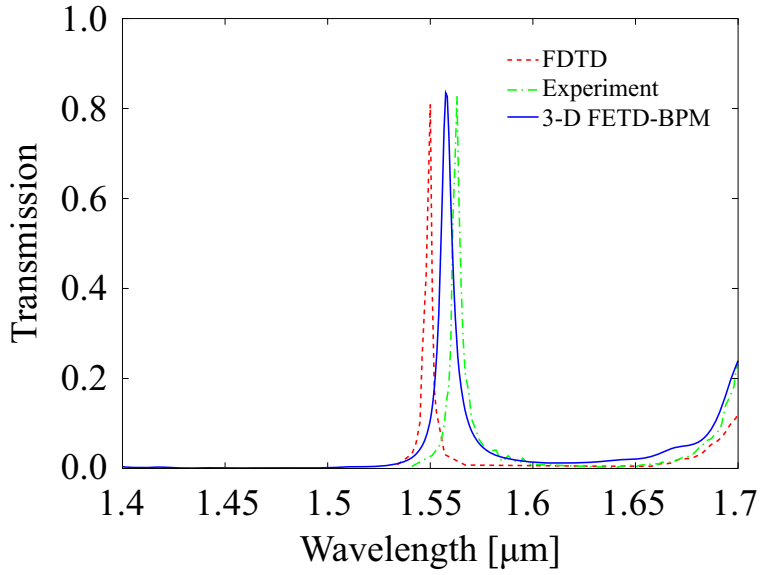

Fig. 6.4. The transmission spectrums of the photonic crystal cavity.

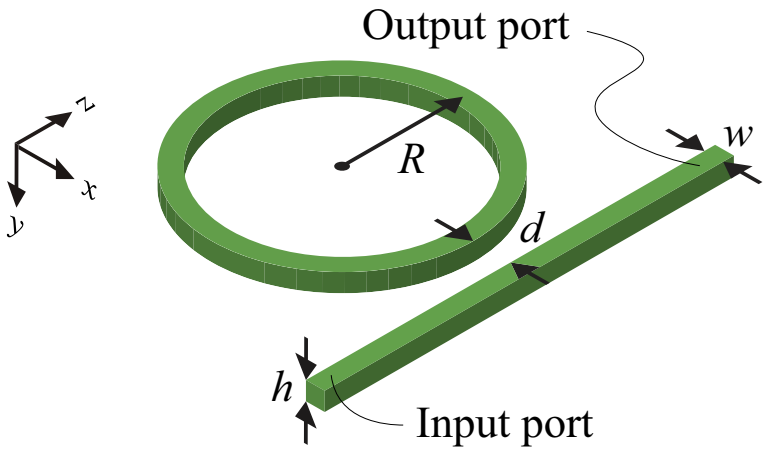

Fig. 6.5. Schematic of a ring resonator.

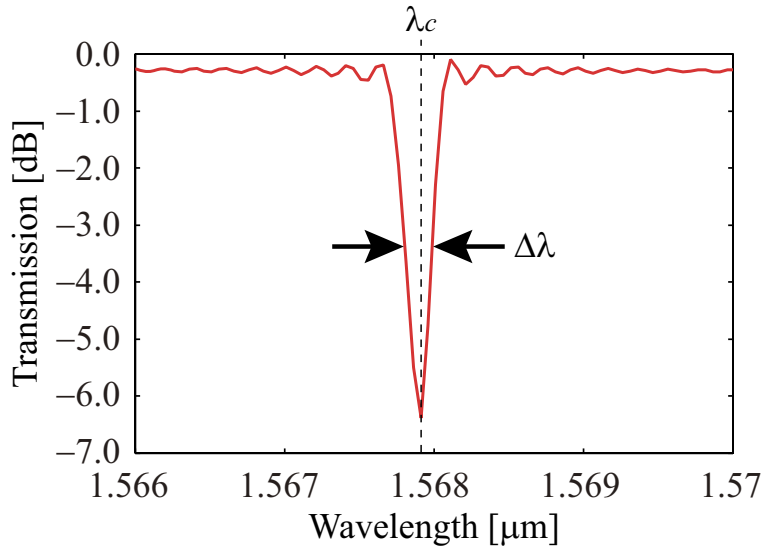

Fig. 6.6. Transmission spectrum of the ring resonator. λ_c and $\Delta\lambda$ represent the resonance wavelength and the FWHM.

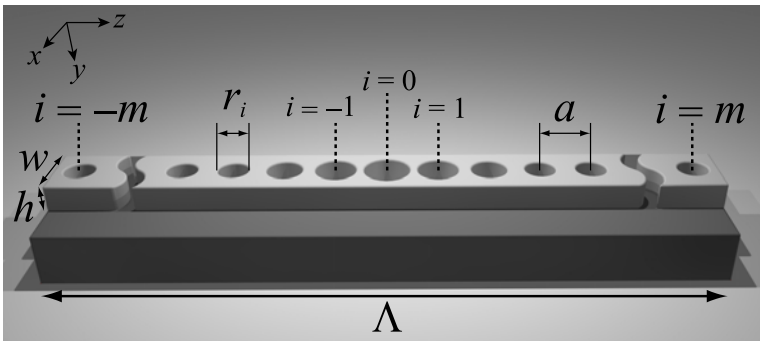

Fig. 6.7. Schematic of a fundamental structure of a 1-D PC-CROW.

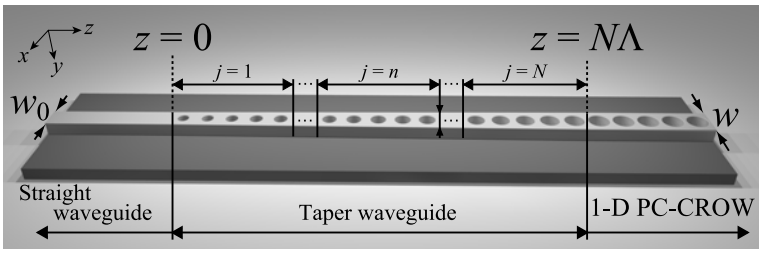

Fig. 6.8. Schematic of a taper waveguide for a highly-efficient connection between a straight waveguide and a 1-D PC-CROW.

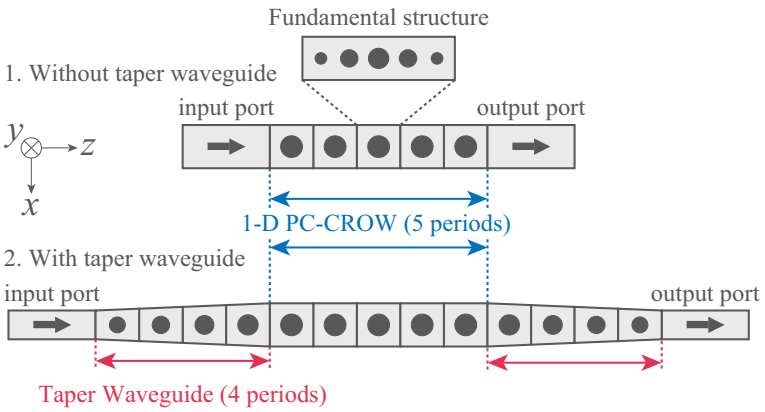

Fig. 6.9. Schematic of an analysis domain.

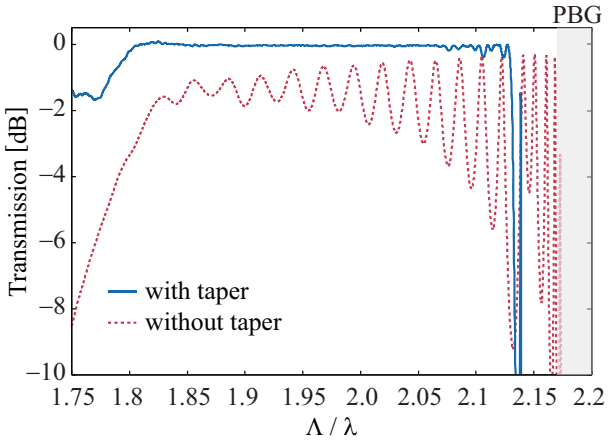

(a)

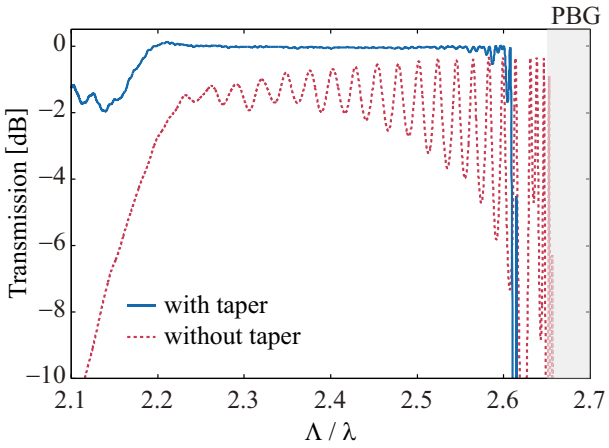

(b)

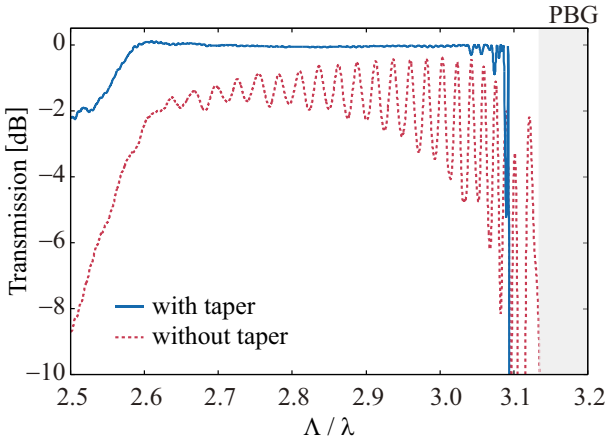

(c)

Fig. 6.10. The transmission characteristics of the 1-D PC-CROW with and without the taper waveguide for (a) $m = 4$, (b) $m = 5$, and (c) $m = 6$.

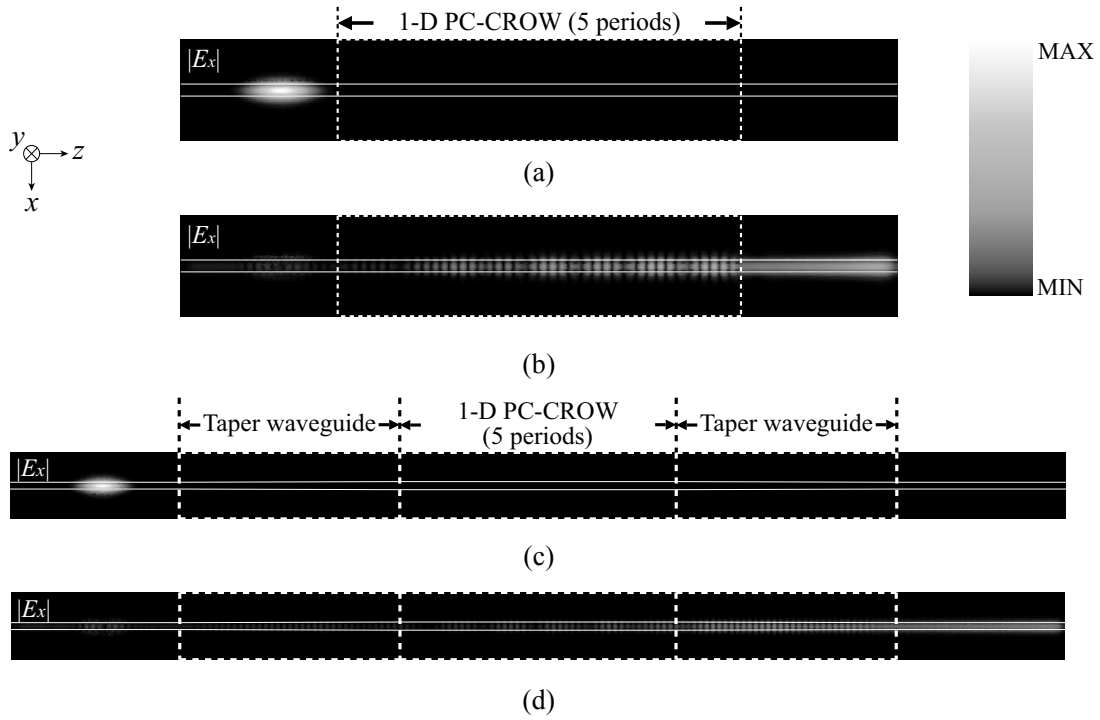

Fig. 6.11. The electric field distribution at the *xy* cross section in the 5-periods 1-D PC-CROW (*m* = 4) without the taper waveguide (a), (b) and with taper waveguide (c), (d). (a), (c) When the optical pulses are launched. (b), (d) When the optical pulses reach the output port.

Chapter 7 Conclusion

The nonlinear optical devices based on 1-D PC cavity is studied for the enhancement of the interactions between the light and the material.

One approach to enhance the light-material interactions is slow light, which is the light with small group velocity. The coupled ring resonator based on the 1-D PC cavity is proposed to realize the small group velocity. The 1-D PC cavity based on the modulated mode-gap is employed to suppress the leakage loss. The decreasing of the group velocity compared with the 1-D PC-CROW is demonstrated. Moreover, the reduction of the number of periods in 90-degree bend section is considered and the advantageous of the 90-degree bend section composed of 2 periods is presented.

Another approach to enhance the nonlinear optical effects is slot waveguides, which can realize the small effective mode area and increase the density of the power of the electromagnetic field. The slot waveguide composed of the 1-D PC cavity is proposed and its nonlinear characteristic is investigated on the basis of the nonlinear coefficient. The numerical results have shown that the maximum nonlinear coefficient of 11 600 $m^{-1}W^{-1}$ is obtained in the optimized structure with width and height of $w = h = 300$ nm. The maximum nonlinear coefficient is not obtained in the structure that achieves the smallest effective mode area or the largest group index. Therefore, the optimum parameters have to be explored for the enhancement of the optical nonlinear effects. Also, there is the trade-off between the nonlinear coefficient and the bandwidth in structure with different number of holes. The nonlinear coefficients can be enlarged by increasing the *m*-value. However, the bandwidth becomes extremely narrow if the overlarge *m*-value is set. Therefore, the *m*-value have to be chosen carefully in terms of the operation bandwidth and the nonlinear coefficient.

Additionally, the coupled resonator optical waveguide based on the slotted 1-D PC cavity was proposed. Its enhancement of the optical nonlinear effects due to the slow-light effect of the CROW and the small effective area of the slotted 1-D PC cavity has been investigated. The trade-off between the nonlinear parameter and the leakage loss was found. To enhance the optical nonlinear effects further, the structure with narrower slot width was investigated and its advantages in terms of both the leakage loss and the nonlinear parameter were demonstrated. Setting the slot length and width appropriately, the largest nonlinear parameter 1.63×10^4 $m^{-1}W^{-1}$ of the CROW based on the slotted 1-D PC cavity can be obtained.

Finally, the taper waveguide for highly-efficient connection between the coupled resonator optical waveguide and the straight waveguide is considered. Since the optical pulse is launched from the straight waveguide to CROW in practice, the taper waveguide is the essential component to realize the highly-efficient connection with the input waveguide over the wide bandwidth. Although a taper

waveguide aiming for a highly-efficient connection is evaluated by 2-D analysis, 3-D analysis has not been reported yet. The 3-D analysis is necessary for the consideration of the radiation to the vertical direction. The 3-D analysis of the taper waveguide is carried out first using the newly developed 3-D FETD-BPM. The highly-efficient connection between the straight waveguide and the CROW structures over the wide bandwidth was demonstrated.

Acknowledgements

I would like to express my sincere appreciation to Professor Kunimasa Saitoh, Division of Media and Network Technologies, Graduate School of Information Science and Technology, Hokkaido University, for the continuing guidance, encouragement, invaluable comments and suggestions during my whole research.

My sincere gratitude goes to Associate Professor Takeshi Fujisawa, Division of Media and Network Technology, Graduate School of Information Science and Technology, Hokkaido University, for the continuing guidance, encouragement, and support through this study.

I am grateful to Professor Yoshikazu Miyanaga, Professor Takeo Ohgane, Division of Media and Network Technology, Graduate School of Information Science and Technology, Hokkaido University, for reviewing and the helpful suggestions.

I also thank all the members in our laboratory for providing the useful suggestions and having the valuable discussions.

References

[1] T. Baba, "Slow light in photonic crystals," *Nat. Photon.,* vol. 2, no. 8, pp. 465-473, Aug. 2008.

[2] T. F. Krauss, "Slow light in photonic crystal waveguides," *J. Phys. D: Appl. Phys.,* vol. 40, no. 9, pp. 2666-2670, Apr. 2007.

[3] T. F. Krauss, "Why do we need slow light?," *Nat. Photon.,* vol. 2, no. 8, pp. 448-450, Aug. 2008.

[4] C. Monat, M. d. Sterke, and B. J. Eggleton, "Slow light enhanced nonlinear optics in periodic structures," *J. Opt.,* vol. 12, no. 10, pp. 104003-104003, Sep. 2010.

[5] Y. Hamachi, S. Kubo, and T. Baba, "Slow light with low dispersion and nonlinear enhancement in a lattice-shifted photonic crystal waveguide," *Opt. Lett.,* vol. 34, no. 7, pp. 1072-1074, Apr. 2009.

[6] K. Inoue, H. Oda, N. Ikeda, and K. Asakawa, "Enhanced third-order nonlinear effects in slow-light photonic-crystal slab waveguides of line-defect," *Opt. Exp.,* vol. 17, no. 9, pp. 7206-7216, Apr. 2009.

[7] C. Monat, B. Corcoran, M. Ebnali-Heidari, C. Grillet, B. J. Eggleton, T. P. White, L. O'Faolain, and T. F. Krauss, "Slow light enhancement of nonlinear effects in silicon engineered photonic crystal waveguides," *Opt. Exp.,* vol. 17, no. 4, pp. 2944-2953, Feb. 2009.

[8] C. Monat, B. Corcoran, D. Pudo, M. Ebnali-Heidari, C. Grillet, M. D. Pelusi, D. J. Moss, B. J. Eggleton, T. P. White, L. O'Faolain, and T. F. Krauss, "Slow light enhanced nonlinear optics in silicon photonic crystal waveguides," *IEEE J. Sel. Topics Quantum Electron.,* vol. 16, no. 1, pp. 344-356, Jan./Feb. 2010.

[9] P. Kanakis, T. Kamalakis, and T. Sphicopoulos, "Designing slow-light photonic crystal waveguides for four-wave mixing applications," *Opt. Lett.,* vol. 39, no. 4, pp. 884-887, Feb. 2014.

[10] J. Li, L. O'Faolain, I. H. Rey, and T. F. Krauss, "Four-wave mixing in photonic crystal waveguides: slow light enhancement and limitations," *Opt. Exp.,* vol. 19, no. 5, pp. 4458-4463, Feb. 2011.

[11] N. Matsuda, H. Takesue, K. Shimizu, Y. Tokura, E. Kuramochi, and M. Notomi, "Slow light enhanced correlated photon pair generation in photonic-crystal coupled-resonator optical waveguides," *Opt. Exp.,* vol. 21, no. 7, pp. 8596-8604, Apr. 2013.

[12] N. Matsuda, T. Kato, K.-i. Harada, H. Takesue, E. Kuramochi, H. Taniyama, and M. Notomi, "Slow light enhanced optical nonlinearity in a silicon photonic crystal coupled-resonator optical waveguide," *Opt. Exp.,* vol. 19, no. 21, pp. 19861-19874, Sep. 2011.

[13] C. Monat, M. Ebnali-Heidari, C. Grillet, B. Corcoran, B. J. Eggleton, T. P. White, L. O'Faolain, J. Li, and T. F. Krauss, "Four-wave mixing in slow light engineered silicon photonic crystal waveguides," *Opt. Exp.,* vol. 18, no. 22, pp. 22915-22927, Oct. 2010.

[14] M. Notomi, "Strong light confinement with periodicity," *Proceedings of the IEEE,* vol. 99, no. 10, pp. 1768-1779, Jun. 2011.

[15] N. Masaya, "Manipulating light with strongly modulated photonic crystals," *Reports on Progress in Physics,* vol. 73, no. 9, pp. 096501-096501, Aug. 2010.

[16] J. D. Joannopoulos, P. R. Villeneuve, and S. Fan, "Photonic crystals: putting a new twist on light," *Nature,* vol. 386, no. 6621, pp. 143-149, Mar. 1997.

[17] T. F. Krauss, R. M. D. L. Rue, and S. Brand, "Two-dimensional photonic-bandgap structures operating at near-infrared wavelengths," *Nature,* vol. 383, no. 6602, pp. 699-702, Oct. 1996.

[18] M. Notomi, K. Yamada, A. Shinya, J. Takahashi, C. Takahashi, and I. Yokohama, "Extremely large group-velocity dispersion of line-defect waveguides in photonic crystal slabs," *Phys. Rev. Lett.,* vol. 87, no. 25, pp. 253902-253902, Nov. 2001.

[19] S. A. Schulz, L. O'Faolain, D. M. Beggs, T. P. White, A. Melloni, and T. F. Krauss, "Dispersion engineered slow light in photonic crystals: a comparison," *J. Opt.,* vol. 12, no. 10, pp. 104004-104004, Sep. 2010.

[20] E. Kuramochi, M. Notomi, S. Hughes, A. Shinya, T. Watanabe, and L. Ramunno, "Disorder-induced scattering loss of line-defect waveguides in photonic crystal slabs," *Phys. Rev. B,* vol. 72, no. 16, pp. 161318-161318, Oct. 2005.

[21] A. Y. Petrov and M. Eich, "Zero dispersion at small group velocities in photonic crystal waveguides," *Appl. Phys. Lett.,* vol. 85, no. 21, pp. 4866-4868, Nov. 2004.

[22] L. H. Frandsen, A. V. Lavrinenko, J. Fage-Pedersen, and P. I. Borel, "Photonic crystal waveguides with semi-slow light and tailored dispersion properties," *Opt. Exp.,* vol. 14, no. 20, pp. 9444-9450, Oct. 2006.

[23] A. Petrov, M. Krause, and M. Eich, "Backscattering and disorder limits in slow light photonic crystal waveguides," *Opt. Exp.,* vol. 17, no. 10, pp. 8676-8684, May 2009.

[24] H. Jin, G. Dingshan, W. Huaming, H. Ran, and Z. Zhiping, "Flat band slow light in symmetric line defect photonic crystal waveguides," *Photon. Technol. Lett.,* vol. 21, no. 20, pp. 1571-1573, Oct. 2009.

[25] D. Mori and T. Baba, "Wideband and low dispersion slow light by chirped photonic crystal coupled waveguide," *Opt. Exp.,* vol. 13, no. 23, pp. 9398-9408, Nov. 2005.

[26] S.-C. Huang, M. Kato, E. Kuramochi, C.-P. Lee, and M. Notomi, "Time-domain and spectral-domain investigation of inflection-point slow-light modes in photonic crystal coupled waveguides," *Opt. Exp.,* vol. 15, no. 6, pp. 3543-3549, Mar. 2007.

[27] T. Kawasaki, D. Mori, and T. Baba, "Experimental observation of slow light in photonic crystal coupled waveguides," *Opt. Exp.,* vol. 15, no. 16, pp. 10274-10281, Aug. 2007.

[28] A. Yariv, Y. Xu, R. K. Lee, and A. Scherer, "Coupled-resonator optical waveguide: a proposal and analysis," *Opt. Lett.,* vol. 24, no. 11, pp. 711-713, Jun. 1999.

[29] S. Olivier, C. Smith, M. Rattier, H. Benisty, C. Weisbuch, T. Krauss, R. Houdré, and U. Oesterlé, "Miniband transmission in a photonic crystal coupled-resonator optical waveguide," *Opt. Lett.,* vol. 26, no. 13, pp. 1019-1021, Jul. 2001.

[30] F. Xia, L. Sekaric, and Y. Vlasov, "Ultracompact optical buffers on a silicon chip," *Nat. Photon.,*

vol. 1, no. 1, pp. 65-71, Dec. 2007.

[31] D. O'Brien, M. D. Settle, T. Karle, A. Michaeli, M. Salib, and T. F. Krauss, "Coupled photonic crystalheterostructure nanocavities," *Opt. Exp.,* vol. 15, no. 3, pp. 1228-1233, Feb. 2007.

[32] M. Notomi, E. Kuramochi, and T. Tanabe, "Large-scale arrays of ultrahigh-Q coupled nanocavities," *Nat. Photon.,* vol. 2, no. 12, pp. 741-747, Nov. 2008.

[33] E. Kuramochi, H. Taniyama, T. Tanabe, K. Kawasaki, Y.-G. Roh, and M. Notomi, "Ultrahigh-Q one-dimensional photonic crystal nanocavities with modulated mode-gap barriers on SiO2 claddings and on air claddings," *Opt. Exp.,* vol. 18, no. 15, pp. 15859-15869, Jul. 2010.

[34] M. Notomi, A. Shinya, S. Mitsugi, E. Kuramochi, and H. Ryu, "Waveguides, resonators and their coupled elements in photonic crystal slabs," *Opt. Exp.,* vol. 12, no. 8, pp. 1551-1561, Apr. 2004.

[35] B.-S. Song, S. Noda, T. Asano, and Y. Akahane, "Ultra-high-Q photonic double-heterostructure nanocavity," *Nature Materials,* vol. 4, no. 3, pp. 207-210, Feb. 2005.

[36] E. Kuramochi, M. Notomi, S. Mitsugi, A. Shinya, T. Tanabe, and T. Watanabe, "Ultrahigh-Q photonic crystal nanocavities realized by the local width modulation of a line defect," *Appl. Phys. Lett.,* vol. 88, no. 4, pp. 041112-041112, Jan. 2006.

[37] Y. Kawaguchi, S. Makino, K. Saitoh, and M. Koshiba, "Structural dependence of group velocity and leakage loss in 1-D photonic crystal coupled resonator optical waveguide with modulated mode-gap," *Photon. J.,* vol. 4, no. 2, pp. 300-309, Apr. 2012.

[38] V. R. Almeida, Q. Xu, C. A. Barrios, and M. Lipson, "Guiding and confining light in void nanostructure," *Opt. Lett.,* vol. 29, no. 11, pp. 1209-1211, Jun. 2004.

[39] Q. Xu, V. R. Almeida, R. R. Panepucci, and M. Lipson, "Experimental demonstration of guiding and confining light in nanometer-sizelow-refractive-index material," *Opt. Lett.,* vol. 29, no. 14, pp. 1626-1628, Jul. 2004.

[40] P. Muellner, M. Wellenzohn, and R. Hainberger, "Nonlinearity of optimized silicon photonic slot waveguides," *Opt. Exp.,* vol. 17, no. 11, pp. 9282-9287, May 2009.

[41] C. Koos, L. Jacome, C. Poulton, J. Leuthold, and W. Freude, "Nonlinear silicon-on-insulator waveguides for all-optical signal processing," *Opt. Exp.,* vol. 15, no. 10, pp. 5976-5990, May 2007.

[42] L. Zhang, Y. Yue, Y. Xiao-Li, J. Wang, R. G. Beausoleil, and A. E. Willner, "Flat and low dispersion in highly nonlinear slot waveguides," *Opt. Exp.,* vol. 18, no. 12, pp. 13187-13193, Jun. 2010.

[43] P. Sanchis, J. Blasco, A. Martinez, and J. Marti, "Design of silicon-based slot waveguide configurations for optimum nonlinear performance," *J. Lightw. Technol.,* vol. 25, no. 5, pp. 1298-1305, May 2007.

[44] T. Vallaitis, S. Bogatscher, L. Alloatti, P. Dumon, R. Baets, M. L. Scimeca, I. Biaggio, F. Diederich, C. Koos, W. Freude, and J. Leuthold, "Optical properties of highly nonlinear silicon-organic hybrid (SOH) waveguide geometries," *Opt. Exp.,* vol. 17, no. 20, pp. 17357-17368, Sep. 2009.

[45] C. Koos, P. Vorreau, T. Vallaitis, P. Dumon, W. Bogaerts, R. Baets, B. Esembeson, BiaggioI, T. Michinobu, F. Diederich, W. Freude, and J. Leuthold, "All-optical high-speed signal processing with silicon-organic hybrid slot waveguides," *Nat. Photon.,* vol. 3, no. 4, pp. 216-219, Apr. 2009.

[46] Z. Xianting, Y. Jinhui, W. Kuiru, K. Zhe, Y. Binbin, S. Xinzhu, W. Qiang, Y. Chongxiu, and G. Farrell, "Strong modulation instability in a silicon organic hybrid slot waveguide," *Photon. J.,* vol. 7, no. 4, pp. 1-8, Jun. 2015.

[47] A. Trita, C. Lacava, P. Minzioni, J.-P. Colonna, P. Gautier, J.-M. Fedeli, and I. Cristiani, "Ultra-high four wave mixing efficiency in slot waveguides with silicon nanocrystals," *Appl. Phys. Lett.,* vol. 99, no. 19, pp. 191105-191105, Nov. 2011.

[48] R. Van Laer, B. Kuyken, D. Van Thourhout, and R. Baets, "Analysis of enhanced stimulated Brillouin scattering in silicon slot waveguides," *Opt. Lett.,* vol. 39, no. 5, pp. 1242-1245, May 2014.

[49] B. Liu, T. Wang, J. Tang, X. Li, C. Dong, and Y. He, "Wideband slow light with low dispersion in asymmetric slotted photonic crystal waveguides," *Appl. Opt.,* vol. 52, no. 34, pp. 8394-8401, Dec. 2013.

[50] L. Yongzhuo, C. Kaiyu, F. Xue, H. Yidong, W. Da, H. Zhilei, and Z. Wei, "Photonic crystal nanobeam cavity with stagger holes for ultrafast directly modulated nano-light-emitting diodes," *Photon. J.,* vol. 5, no. 1, pp. 4700306-4700306, Jan. 2013.

[51] P. Seidler, K. Lister, U. Drechsler, J. Hofrichter, and T. Stöferle, "Slotted photonic crystal nanobeam cavity with an ultrahigh quality factor-to-mode volume ratio," *Opt. Exp.,* vol. 21, no. 26, pp. 32468-32483, Dec. 2013.

[52] Q. Biao, Y. Ping, L. Yubo, J. Xiaoqing, Y. Mei, and Y. Jianyi, "Analysis of electrooptic modulator with 1-D slotted photonic crystal nanobeam cavity," *Photon. Technol. Lett.,* vol. 23, no. 14, pp. 992-994, Jul. 2011.

[53] K. Li, J. Li, Y. Song, G. Fang, C. Li, Z. Feng, R. Su, B. Zeng, X. Wang, and C. Jin, "L_n slot photonic crystal microcavity for refractive index gas sensing," *Photon. J.,* vol. 6, no. 5, pp. 1-9, Oct. 2014.

[54] C. Caër, X. Le Roux, and E. Cassan, "High-Q silicon-on-insulator slot photonic crystal cavity infiltrated by a liquid," *Appl. Phys. Lett.,* vol. 103, no. 25, pp. 251106-251106, Dec. 2013.

[55] C. Schriever, C. Bohley, and J. Schilling, "Designing the quality factor of infiltrated photonic wire slot microcavities," *Opt. Exp.,* vol. 18, no. 24, pp. 25217-25224, Nov. 2010.

[56] T. Yamamoto, M. Notomi, H. Taniyama, E. Kuramochi, Y. Yoshikawa, Y. Torii, and T. Kuga, "Design of a high-Q air-slot cavity based on a width-modulated line-defect in a photonic crystal slab," *Opt. Exp.,* vol. 16, no. 18, pp. 13809-13817, Sep. 2008.

[57] P. Yu, B. Qi, X. Jiang, M. Wang, and J. Yang, "Ultrasmall-V high-Q photonic crystal nanobeam microcavities based on slot and hollow-core waveguides," *Opt. Lett.,* vol. 36, no. 8, pp. 1314-1316,

Apr. 2011.

[58] C. Caer, X. Le Roux, D. Van Khanh, D. Marris-Morini, N. Izard, L. Vivien, G. Dingshan, and E. Cassan, "Dispersion engineering of wide slot photonic crystal waveguides by bragg-like corrugation of the slot," *Photon. Technol. Lett.,* vol. 23, no. 18, pp. 1298-1300, Sep. 2011.

[59] D. Mascoli, D. Gerace, and L. C. Andreani, "Q-factor optimization for TM-like modes in pillar-based photonic crystal cavities with planar slot waveguides," *Photonics and Nanostructures - Fundamentals and Applications,* vol. 9, no. 1, pp. 63-69, Oct. 2011.

[60] Q. Biao, Y. Ping, L. Yubo, H. Yinlei, Z. Qiang, J. Xiaoqing, and Y. Jianyi, "Ultracompact electrooptic silicon modulator with horizontal photonic crystal slotted slab," *Photon. Technol. Lett.,* vol. 22, no. 10, pp. 724-726, May 2010.

[61] T.-W. Lu, P.-T. Lin, and P.-T. Lee, "Photonic crystal horizontally slotted nanobeam cavity for silicon-based nanolasers," *Opt. Lett.,* vol. 37, no. 4, pp. 569-571, Feb. 2012.

[62] J. Jágerská, H. Zhang, Z. Diao, N. L. Thomas, and R. Houdré, "Refractive index sensing with an air-slot photonic crystal nanocavity," *Opt. Lett.,* vol. 35, no. 15, pp. 2523-2525, Aug. 2010.

[63] J. Wu, Y. Li, C. Peng, and Z. Wang, "Wideband and low dispersion slow light in slotted photonic crystal waveguide," *Opt. Comm.,* vol. 283, no. 14, pp. 2815-2819, Jul. 2010.

[64] J. D. Ryckman and S. M. Weiss, "Low mode volume slotted photonic crystal single nanobeam cavity," *Appl. Phys. Lett.,* vol. 101, no. 7, pp. 071104-071104, Aug. 2012.

[65] J. D. Ryckman and S. M. Weiss, "Localized field enhancements in guided and defect modes of a periodic slot waveguide," *Photon. J.,* vol. 3, no. 6, pp. 986-995, Oct. 2011.

[66] K. Foubert, L. Lalouat, B. Cluzel, E. Picard, D. Peyrade, F. de Fornel, and E. Hadji, "An air-slotted nanoresonator relying on coupled high Q small V Fabry–Perot nanocavities," *Appl. Phys. Lett.,* vol. 94, no. 25, pp. 251111-251111, Jun. 2009.

[67] C. Caer, X. Le Roux, and E. Cassan, "Enhanced localization of light in slow wave slot photonic crystal waveguides," *Opt. Lett.,* vol. 37, no. 17, pp. 3660-3662, Sep. 2012.

[68] J. H. Wülbern, J. Hampe, A. Petrov, M. Eich, J. Luo, A. K.-Y. Jen, A. Di Falco, T. F. Krauss, and J. Bruns, "Electro-optic modulation in slotted resonant photonic crystal heterostructures," *Appl. Phys. Lett.,* vol. 94, no. 24, pp. 241107-241107, Jun. 2009.

[69] A. Di Falco, L. O'Faolain, and T. F. Krauss, "Dispersion control and slow light in slotted photonic crystal waveguides," *Appl. Phys. Lett.,* vol. 92, no. 8, pp. 083501-083501, Feb. 2008.

[70] Y. Li, J. Zheng, J. Gao, J. Shu, M. S. Aras, and C. W. Wong, "Design of dispersive optomechanical coupling and cooling in ultrahigh-Q/V slot-type photonic crystal cavities," *Opt. Exp.,* vol. 18, no. 23, pp. 23844-23856, Nov. 2010.

[71] J. Gao, J. F. McMillan, M.-C. Wu, J. Zheng, S. Assefa, and C. W. Wong, "Demonstration of an air-slot mode-gap confined photonic crystal slab nanocavity with ultrasmall mode volumes," *Appl. Phys. Lett.,* vol. 96, no. 5, p. 051123, Feb. 2010.

[72] B. Wang, M. A. Dündar, R. Nötzel, F. Karouta, S. He, and R. W. van der Heijden, "Photonic crystal slot nanobeam slow light waveguides for refractive index sensing," *Appl. Phys. Lett.,* vol. 97, no. 15, pp. 151105-151105, Oct. 2010.

[73] F. Riboli, P. Bettotti, and L. Pavesi, "Band gap characterization and slow light effects in one dimensional photonic crystals based on silicon slot-waveguides," *Opt. Exp.,* vol. 15, no. 19, pp. 11769-11775, Sep. 2007.

[74] J.-M. Brosi, C. Koos, L. C. Andreani, M. Waldow, J. Leuthold, and W. Freude, "High-speed low-voltage electro-optic modulator with a polymer-infiltrated silicon photonic crystal waveguide," *Opt. Exp.,* vol. 16, no. 6, pp. 4177-4191, Mar. 2008.

[75] W.-C. Lai, S. Chakravarty, X. Wang, C. Lin, and R. T. Chen, "Photonic crystal slot waveguide absorption spectrometer for on-chip near-infrared spectroscopy of xylene in water," *Appl. Phys. Lett.,* vol. 98, no. 2, pp. 023304-023304, Jan. 2011.

[76] Y. Kawaguchi, K. Saitoh, and M. Koshiba, "Design of taper structure for highly efficient coupling between 1-D photonic crystal coupled resonator optical waveguide and straight waveguide," *J. Lightw. Technol.,* vol. 27, no. 14, pp. 2924-2929, Jul. 2009.

[77] Y. Tsuji and M. Koshiba, "Finite element method using port truncation by perfectly matched layer boundary conditions for optical waveguide discontinuity problems," *J. Lightw. Technol.,* vol. 20, no. 3, pp. 463-468, Mar. 2002.

[78] N. Kono and M. Koshiba, "Three-dimensional finite element analysis of nonreciprocal phase shifts in magneto-photonic crystal waveguides," *Opt. Exp.,* vol. 13, no. 23, pp. 9155-9166, Nov. 2005.

[79] K. C. Huang, E. Lidorikis, X. Jiang, J. D. Joannopoulos, K. A. Nelson, P. Bienstman, and S. Fan, "Nature of lossy Bloch states in polaritonic photonic crystals," *Phys. Rev. B,* vol. 69, no. 19, pp. 195111-195111, May 2004.

[80] T. Sato, S. Makino, Y. Ishizaka, T. Fujisawa, and K. Saitoh, "Three-dimensional finite-element mode-solver for nonlinear periodic optical waveguides and its application to photonic crystal waveguides," *J. Lightw. Technol.,* vol. 32, no. 21, pp. 4011-4019, Nov. 2014.

[81] B. Esembeson, M. L. Scimeca, T. Michinobu, F. Diederich, and I. Biaggio, "A high-optical quality supramolecular assembly for third-order integrated nonlinear optics," *Adv. Mater.,* vol. 20, no. 23, pp. 4584-4587, Oct. 2008.

[82] M. Koshiba and Y. Tsuji, "Curvilinear hybrid edge/nodal elements with triangular shape for guided-wave problems," *J. Lightw. Technol.,* vol. 18, no. 5, pp. 737-743, May 2000.

[83] T. Sato, S. Makino, Y. Ishizaka, T. Fujisawa, and K. Saitoh, "A rigorous definition of nonlinear parameter γ and effective area A_{eff} for photonic crystal optical waveguides," *J. Opt. Soc. Am. B,* vol. 32, no. 6, pp. 1245-1251, Jun. 2015.

[84] G. R. Hadley, "Wide-angle beam propagation using Padé approximant operators," *Opt. Lett.,* vol. 17, no. 20, pp. 1426-1428, Oct. 1992.

[85] J. S. Foresi, P. R. Villeneuve, J. Ferrera, E. R. Thoen, G. Steinmeyer, S. Fan, J. D. Joannopoulos, L. C. Kimerling, H. I. Smith, and E. P. Ippen, "Photonic-bandgap microcavities in optical waveguides," *Nature,* vol. 390, no. 6656, pp. 143-145, Nov. 1997.

[86] Q. Xu and M. Lipson, "All-optical logic based on silicon micro-ring resonators," *Opt. Exp.,* vol. 15, no. 3, pp. 924-929, Feb. 2007.

Copyright notice

List of Author's Publication

1. Papers

[1] S. Makino, T. Fujisawa, and K. Saitoh, "Enhancement of Optical Nonlinearity in Coupled Resonator Optical Waveguide Based on Slotted 1-D Photonic Crystal Cavity," *IEEE Photonics Journal*, vol. 7, no. 6, pp. 4501608, Dec. 2015.

[2] S. Makino, T. Sato, Y. Ishizaka, T. Fujisawa, and K. Saitoh, "Three-dimensional finite-element time-domain beam propagation method and its application to 1-D photonic crystal coupled resonator optical waveguide," *IEEE/OSA Journal of Lightwave Technology*, vol. 33, no. 18, pp. 3836-3842, Spt. 2015.

[3] S. Makino, Y. Ishizaka, Y. Kawaguchi, K. Saitoh, and M. Koshiba, "Proposal of coupled ring resonator based on one-dimensional photonic crystal nanocavity," *IEEE/OSA Journal of Lightwave Technology*, vol. 31, no. 15, pp. 2565-2569, Aug. 2013

[4] S. Makino, Y. Ishizaka, K. Saitoh, and M. Koshiba, "Slow-light-enhanced nonlinear characteristics in slot waveguides composed of photonic crystal nanobeam cavities," *IEEE Photonics Journal*, vol. 5, no. 2, pp. 2700309, Apr. 2013.

2. International conferences

[1] S. Makino, Y. Ishizaka, K.Saitoh, M. Koshiba, "Structural dependence of nonlinear characteristics in coupled resonator optical waveguides based on slotted nanobeam cavities," Frontiers in Optics (FiO 2013), FW4E.5, Florida, USA, Oct. 2013.

[2] S. Makino, Y. Ishizaka, K.Saitoh, M. Koshiba, "A proposal of coupled resonator optical waveguides based on slotted nanobeam cavities," Summer Topicals (SUM 2013), TuA4.6, Hawaii, USA, Jul. 2013.

[3] S. Makino, Y. Ishizaka, K. Saitoh, M. Koshiba, "Structural dependence of nonlinear characteristics in slot waveguides composed of photonic crystal nanobeam cavities," Conference on Lasers and Electro-Optics Pacific Rim, and OptoElectronics and Communications Conference / Photonics in Switching (CLEO-PR&OECC/PS 2013), TuPI-4, Kyoto, Japan , Jun. 2013.

[4] S. Makino, Y. Kawaguchi, K. Saitoh, and M. Koshiba, "A proposal of doubly coupled resonator optical waveguides," OptoElectronics and Communications Conference (OECC 2012), P2-19, Busan, Korea, Jul. 2012.

[5] S. Makino, Y. Kawaguchi, K. Saitoh, and M. Koshiba, "Design of doubly coupled resonator

optical waveguides," Integrated Photonics Research, Silicon and Nano-Photonics (IPR 2012), JTu5A.9, Colorado, USA, Jun. 2012.

3. Domestic conferences

[1] S. Makino, Y. Ishizaka, T. Fujisawa, and K. Saitoh, "Investigation of a taper waveguide for a highly-efficient connection between 1-D PC-CROW and straight waveguide," Proceedings of the 2014 IEICE Society Conference, C-3-43, 2014. (in Japanese).

[2] S. Makino, Y. Ishizaka, K. Saitoh, and M. Koshiba, "Investigation of Nonlinear Characteristics in Coupled Resonator Optical Waveguides Based on Slotted Nanobeam Cavities," Proceedings of the 2013 IEICE Society Conference, C-3-7, Sep. 2013. (in Japanese).

[3] S. Makino, Y. Ishizaka, K. Saitoh, and M. Koshiba, "Investigation of Nonlinear Characteristics in Slot Waveguides Composed of 1-D PC-CROWs," Proceedings of the 2013 IEICE General Conference, C-3-47, Mar. 2013. (in Japanese).

[4] S. Makino, Y. Ishizaka, K. Saitoh, and M. Koshiba, "Investigation of Nonlinear Characteristics of 1-D Photonic Crystal Coupled Resonator Optical Waveguides," Proceedings of the 2012 IEICE Society Conference, C-3-46, Sep. 2012. (in Japanese).

[5] S. Makino, Y. Kawaguchi, K. Saitoh, and M. Koshiba, "Investigation of Coupling Characteristics in 1-D Photonic Crystal Coupled Resonator Optical Waveguides," Proceedings of the 2012 IEICE General Conference, C-3-73, Mar. 2012. (in Japanese).